



LAWRENCE
LIVERMORE
NATIONAL
LABORATORY

Combined infrared thermal imaging and laser heating for the study of materials thermophysical and processing properties at high temperatures

S. Elhadj, M. J. Matthews, S. T. Yang

September 24, 2012

Critical Reviews in Solid State and Materials Sciences

Disclaimer

This document was prepared as an account of work sponsored by an agency of the United States government. Neither the United States government nor Lawrence Livermore National Security, LLC, nor any of their employees makes any warranty, expressed or implied, or assumes any legal liability or responsibility for the accuracy, completeness, or usefulness of any information, apparatus, product, or process disclosed, or represents that its use would not infringe privately owned rights. Reference herein to any specific commercial product, process, or service by trade name, trademark, manufacturer, or otherwise does not necessarily constitute or imply its endorsement, recommendation, or favoring by the United States government or Lawrence Livermore National Security, LLC. The views and opinions of authors expressed herein do not necessarily state or reflect those of the United States government or Lawrence Livermore National Security, LLC, and shall not be used for advertising or product endorsement purposes.

Combined infrared thermal imaging and laser heating for the study of materials thermophysical and processing properties at high temperatures

Selim Elhadj, Manyalibo J. Matthews, Steven T. Yang

Lawrence Livermore National Laboratory, Livermore, California 94550, USA

Correspondence should be addressed to Selim Elhadj, Elhadj2@llnl.gov

Focused laser irradiation can easily drive materials to extreme temperatures with very high precision and control. In combination with infrared imaging and material characterization techniques, the resulting thermal load can be assessed to derive meaningful thermophysical properties avoiding interferences that would normally occur with direct contact measurements of temperature. In this focused review we first address technical challenges with the experimental implementation involved in obtaining laser-induced temperature field data from infrared imaging. We then discuss suitable heat transport models for analysis of thermal data and, finally, describe specific examples of thermophysical material parameters derived from combined infrared imaging and laser heating. The aim is to illustrate general principles of this combined laser-based heating and IR thermal imaging approach that are useful for experimentation under extreme conditions, which often remain out of reach of conventional methods.

1. Introduction

Laser-matter interactions at surfaces are relevant to a broad array of industrial and research areas, including material processing and analytical chemistry. In industrial settings, laser-based machining and texturing [1], laser annealing [2], and laser-based cleaning [3] are routine. Many analytical techniques rely on laser driven energy deposition for sampling, such as laser ablation-inductively coupled plasma-mass spectroscopy [4-6], or use lasers for interrogating the surface directly (e.g. second-harmonic generation [7]) while carefully *avoiding* heating. Finally, micro-fabrication by laser assisted material deposition relies on lasers heating to induce localized precursor polymerization on a substrate. A great feature of lasers that make them such ubiquitous processing and probing tools is that the volume of analysis or treatment is generally confined to the footprint of the laser beam size with a resolution on the order of the diffraction limit of the laser wavelength (λ_L), although near-field focusing with particle arrays has been demonstrated [8]. Nevertheless, the size of the heat affected zone extends beyond the beam absorption depth $\delta = \alpha^{-1}$ at λ_L (α is the absorption coefficient in μm^{-1}) depending on the thermal diffusion length $\sim \sqrt{t_{\text{exp}} D}$, where t_{exp} is the laser exposure time, and D is the bulk thermal diffusion constant. For short exposure times, low thermal diffusivity, and optically thick (small δ) materials, the heat affected zone is mostly confined to a surface area scaled by the laser irradiance profile. Therefore

the area processed by a laser beam under these conditions is generally more deterministic and localized compared to other heating techniques such as flame, resistive, induction, or electrical arc heating.

Lasers can also impart large amounts of energy at virtually limitless rates which translate into very high heating rates (10^3 - 10^{10} K/s) within an effective absorption depth by either direct phonon coupling or by a two step process using ultra-short pulses [9-11]. The latter occurs first as the radiation field interacts with the electrons on the time scales \approx femtosecond [10], followed by thermalization when the laser pulse width is on the order of the electron-phonon interaction time (\approx 10's of ps). By using very short pulses <10 ps material is removed faster than heat can be transferred to the bulk and little collateral damage will occur even if the temperature in the plume of the ablated material is elevated >1 eV [12]. This nearly "athermal" approach limits residual stress, melted zone depth and flow, and any process where structural relaxation is thermally activated [11]. In contrast, longer pulses will heat the surface and a larger portion of the bulk within a heat affected zone, reaching T far greater than by most other conventional heating methods. For routine, technologically relevant applications these T extend up to ≈ 5000 K, near the boiling point of the toughest materials used for flight and nuclear applications for example. Hence lasers are favored in applications involving hard to machine parts (ex. ceramics, diamond, SiC, etc.), doing so with virtually no wear. In particular, laser parameters can improve process control because they can be very finely tuned to a particular target process [13, 14]. This way, deterministic heating becomes a simple matter of adjusting laser parameters such as wavelength, beam size, exposure time, power, temporal and spatial shape, and pulse repetition frequency. The availability of high power lasers enables experimentations above the current ≈ 2000 °C limit set by the typical containment vessel inertness [15]. For conductor materials, fast dynamic methods with resistive self-heating are usually employed to get around this problem but this approach limits the range of materials that can be interrogated [16]. With focused beam application however, the sample being tested essentially acts as its own containment vessel, avoiding any wall contaminants, and virtually without affecting the surroundings because only a small part of the material is being treated.

Still, an understanding of any of the phenomena resulting from laser irradiation almost certainly requires a measurement of the T evolution for at least two reasons. First, most material properties and thermo-mechanical response are T dependent, second, most phenomena such as pyrolytic reactions, sintering, phase transitions, material flow, structural relaxation, are thermally activated. In other words, T is the main driving force for many important laser-induced material transformations. Even modeling such processes requires knowledge of the T field and history, but such information is difficult to derive *a priori* from the complete conservation equations because of the large number of potential heat dissipative processes that limit the T [17-20]. A simple example of laser machining above the evaporation or ablation threshold illustrates this point. Following energy deposition from laser absorption, heat transport and energy coupling can involve - simultaneously - thermal conduction to the substrate, radiation transport, evaporation, mass transport dynamics, heat convection to the surroundings and, at very high T , plasma generation near the irradiated surface, which can dynamically deflect the laser power from the absorbing surface. The changing shape of the surface will also determine the laser coupling since reflectivity is generally a steep function of incidence angle. Thus, any quantitative modeling effort needs to account for these complex and highly coupled processes. In

reality such modeling is nearly impossible because the thermophysical properties on which they depend are unknown, especially at T above where furnaces can be used for experimentation. The approach to address this issue becomes that of determining individually each of the processes by a combination of experimentation and modeling in the T regime where, for example, radiation transport can be neglected [21], or where evaporative losses are much smaller than thermal conduction [17]. Still, such methods need reliable T measurement to validate the model and to properly account for the experimental observations.

Typical laser applications use a focused beam on micrometer length scales with radial T gradient on the order of 10^2 - 10^4 Kmm⁻¹ causing large hydrodynamic flow. Thus T measurements involving a probe contact with a surface are not ideal because they have the potential to both interfere with the laser irradiation of the surface, and act as a heat sink distorting the T field. Suitable contact of the probe with surface to be measured is also highly problematic and limits the temporal resolution of the measurement (> 10 ms) and to T smaller than about 2500K (for W/W Re alloy thermocouples). In contrast, a radiometric method for surface T determination is ideal for four reasons: 1) it is non-invasive and non-obstructive as it instantaneously looks at emitted radiation, 2) it can produce high temporal resolution T data depending on the detector bandwidth, 3) it can, in principle, achieve single photon level sensitivity, with a dynamic range as broad as the data acquisition, optical setup, and detector will allow [22, 23], 4) as noted earlier, radiometry can have micron scale resolution depending on the optical and detector configuration. Most other direct-contact T measurements fail in one way or the other in such regards [15, 24], while other types of non-contact optical techniques, such as Raman scattering, are usually restricted by background thermal emissions, slower capture rates from signal averaging, and by increased system complexity from the added pump laser [25, 26].

Therefore the intersection of laser processing and thermal infrared (IR) surface imaging offers an ideal experimental system that is particularly well suited for probing rapid laser-induced phenomena, on the micron length scales, and under extreme conditions where most vessels used for experimentation would fail, or where rapid and controlled heating would be difficult. This approach is not without technical and analytical challenges, which will be addressed in this focused review. Particularly, the non-isothermal conditions inherent to laser point source heating can make interpretation of results difficult, but not impossible with the appropriate models. In situations where the T dependence of the processes scrutinized is very strong or where the appropriate thermal model of the laser heating is used, consideration of the peak T alone is sufficient for analysis. Therefore, it is the intention of this review to illustrate how IR surface imaging in combination with laser coupling can be effectively used to derive thermophysical material properties under extreme conditions otherwise not attainable (Salikhov 1999, Boivineau 2006). In general, this insight has not been recognized in the literature. We describe here an approach for analysis of laser heated surfaces with an emphasis on infrared imaging as a tool to obtain T measurements that can be used to derive meaningful thermophysical properties. To illustrate the approach, this review focuses mostly on a few examples and experimental model systems from the literature dealing with fused silica, an important optical material whose inertness and high working point makes it especially difficult to process thermally. In those examples we describe how thermal IR imaging was applied to derive thermophysical properties. However, the experimental and analytical

principles described here should remain broadly applicable to a large number of research areas in the fields of material science, where thermal processes are important, and where extreme T limit use of conventional experimental methods.

2. An optimization of IR thermography for temperature measurements of laser heated surfaces

Although a range of optical measurement systems can be used to determine surface T [24], we only address here IR thermography based on IR focal plane array (FPA) detectors. Because of the high emissivity of most materials in the IR, IR camera systems can more easily be implemented to derive spatially and temporally resolved T measurements. In addition, recent advances in large multispectral IR FPA's ($\approx 10^6$ pixel arrays) promise to deliver even greater measurement integration and capability (Rogalski 2009). Some of the attractive features of these new systems are that the material emissivity may not be required (see a review on multi-color pyrometry [24]), the optical collection system can be made much simpler, and capture rates can be much higher than those based on spectrometric measurements. Here we describe a near-monochromatic IR detection system. However, since IR-based techniques rely on the same principles of thermal emission radiometry, the same consideration presented here should apply to other implementations of thermal IR imaging.

2.1. Description of an optical setup for combined in situ IR measurements and laser heating

Figure 1 below shows a simple laser heating-optical configuration to derive spatially and temporally resolved T measurements *in situ*.

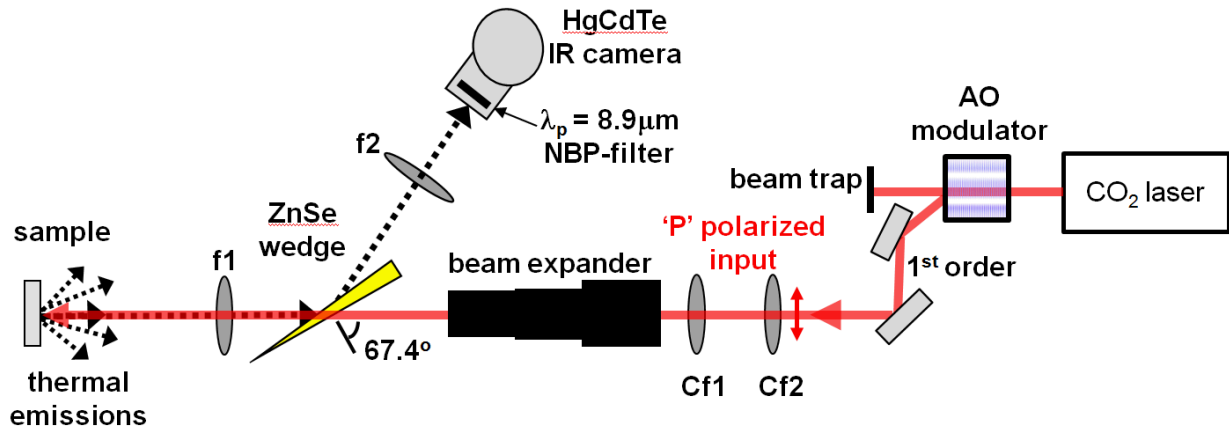


Figure 1. IR optical camera and laser setup for in situ surface temperature measurements and sample heating. Cf1, Cf2, f1, and f2 are ZnSe lenses; a beam expander telescope with variable magnification; NBP is the narrow-bandpass cold filter residing inside the LN HgCdTe (MCT) cooled camera centered at 8.9 μm placed immediately in front of the camera detector.

There are three main features to this setup. First, there is a Mercury Telluride Cadmium (HgCdTe or MCT) camera capable of detection from the near IR (NIR) up to long wave IR (LWIR) $\sim 2\text{-}12 \mu\text{m}$ with a 256×256 element focal plane array (maximum of 33 fps). The analog output of the FPA is converted into 14-bit digital output from the camera for digital processing. A cold narrow-bandpass filter is used inside

the LN-cooled camera to remove any ambient radiation sources, laser light reflection, and to dial the probe wavelength, λ_p , to the particular material absorption peak as discussed below. Keeping the filter cold reduces significantly the ambient thermal noise which has peak emissions around 10 μm at room T . Second, the CO_2 laser beam shown can be relayed, expanded, and focused on the surface with the lenses indicated without any interference in the laser beam path thanks to a ZnSe wedge that allows the polarized beam to pass, while also steering the IR thermal emissions from the surface to the camera FPA. The wedge is oriented at Brewster's angle (67.4°) to pass the p-polarized 10.6 μm laser light while reflecting 50% of the 'S' polarized fraction of the blackbody emission collected from the heated surface by the final focusing lens (f1) and imaged on the FPA by another lens (f2). A significant advantage of using a wedge in this fashion is that it allows viewing of the sample at normal incidence since the emissivity of a surface is angle dependent [27] and many emissivity measurements are reported for normal incidence (and generally remain constant to about 30° half angle). In addition, the same optical system that is used to focus the laser on the surface is also used to collect the thermal emission steered with the wedge. This greatly lowers the system complexity and assures good spatial registration between the heated and measured areas. A third part of the setup includes the acousto-optic (AO) modulator used to modulate the power delivered to the sample, and to enable time-dependent studies when probe measurements are synchronized to the thermal camera. The integrated IR camera – laser setup shown in Fig. 1 represents the basis for an experimental model system applied to the study of materials thermophysical properties at high T . Additional characterization diagnostics of the surface or plume can be included with a probe beam parallel to the sample surface, or at an angle (not shown). A beam diagnostic-leg can also be included to monitor the laser power, or for closed-loop feedback control of the laser power. Finally, in studies involving assist or reactive gas application discussed later, a nozzle with a transparent back-window can be included in the laser beam path within the space in front of the sample as described elsewhere in details [28]. An example of a thermal IR image from a CO_2 laser heated silica surface is shown in Fig. 2(A), while the corresponding surface T profile is shown in Fig. 2(B) using the setup in Fig. 1. Below, we describe the experimental procedure and analytical tool used to produce these IR-based T measurements.

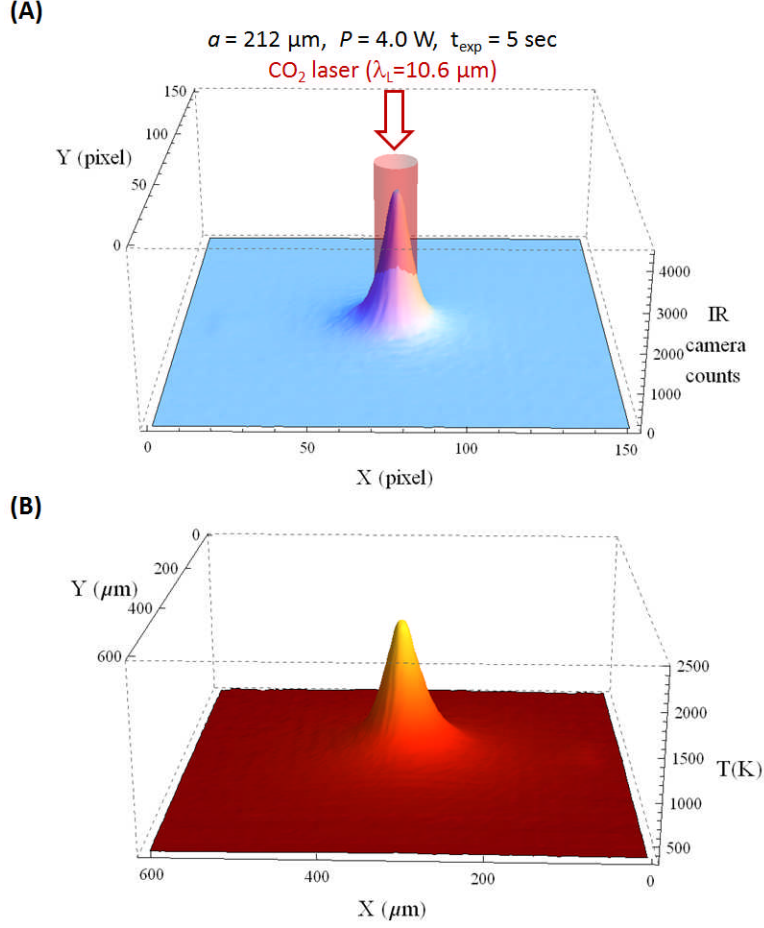


Figure 2. (A) Measured IR camera counts resulting from a CO_2 laser exposure with beam parameters indicated. The cylinder depicts the Gaussian laser beam with $1/e$ Gaussian radius, a , with power, P , and exposure time, t_{exp} . (B) The corresponding temperature surface profile near the end of the laser exposure is based on the calibrated thermal emission flux measurement from a blackbody source (section 2.3).

2.2. Selecting the probe IR wavelengths

When measuring outer surface T of laser heated samples, a critical issue is selecting an “optimal” probe wavelength, λ_p . The relevant wavelengths are all in the IR bands shown in Fig. 3(A), where most of the thermal emission peaks are located, except for the most extreme $T > 5000\text{K}$, where the peaks are shifted down to the visible wavelengths and beyond. A range of commercial FPA detectors are available to probe from 2-20 μm , including InSb, HgCdTe, PtSi, InGaAs and GaAs/AlGaAs quantum wells photodetectors (see a review by Rogalski on recent IR detectors [29]). Thus the entire IR spectrum can in principle be probed depending on the sample thermo-optical properties, T expected, and constraints from the experimental configuration.

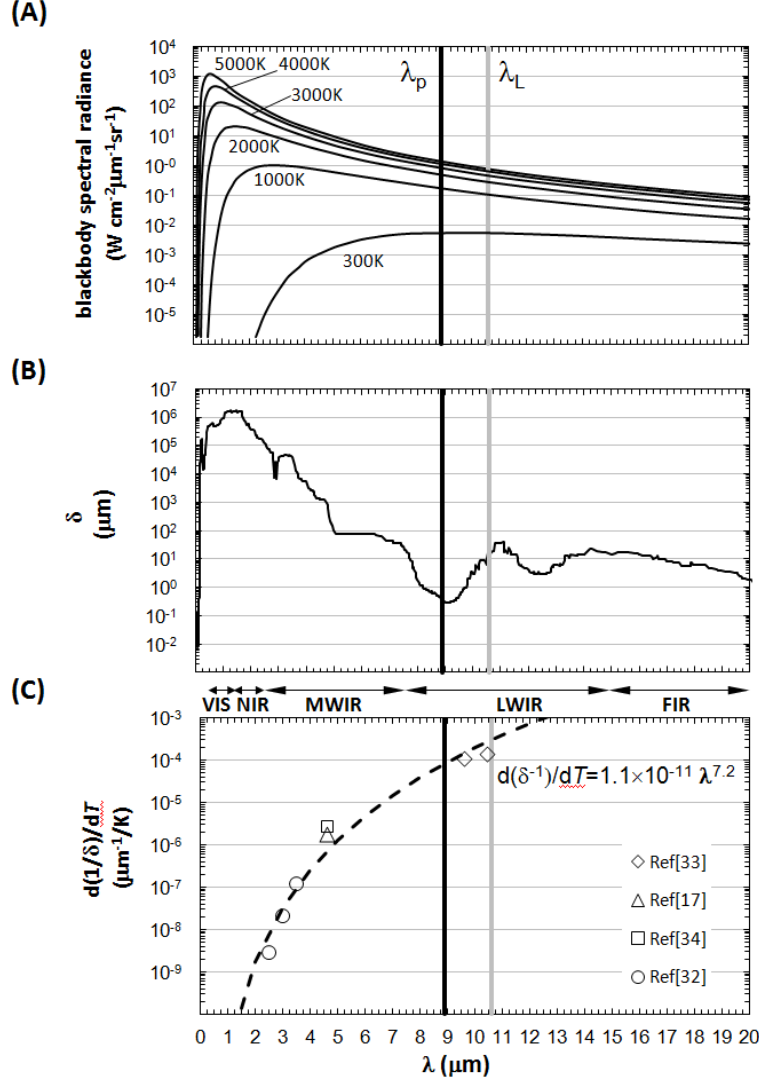


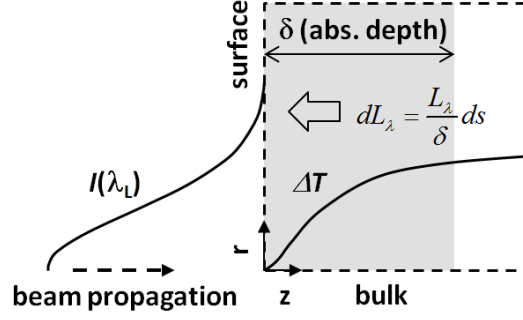
Figure 3. (A) Calculated Planck spectral radiance, L_{λ} , of a blackbody at the given temperatures for the visible (VIS) and various infrared bands delineated by the arrows. (B) Room temperature absorption depth spectra of fused silica derived from Ref[43]. The absorption coefficient is the inverse of the absorption depth $\sim 1/\delta$. (C) Temperature dependence of fused silica absorption coefficient extracted from extinction coefficient data, $\kappa(T)$, measured at discrete wavelengths in the references indicated. The absorption coefficient at a particular λ , $1/\delta$, is related to the κ by, $1/\delta = 4\pi\kappa/\lambda$. The temperature dependence of the absorption coefficient data in (C) appears to follow an empirical power law relation as indicated by the least square fit (dashed curve). The vertical black band in each of the plots in (A), (B), (C) represents a probe wavelength, λ_p , used with an IR imaging system. The grey band represents the laser wavelength, λ_L , used for efficient (small δ) heating of fused silica.

Although the relative error of the measured T generally scales with λ_p , the optimal probe wavelength should ideally i) be within the range of wavelengths where the T dependent emissivity, $\epsilon(T)$, of the surface is known, ii) be close to the peak sensitivity of the FPA, iii) be in the range that excludes both laser light reflected from the surface and ambient radiation (Fig. 3(A)) iv) and, most importantly, probe at a wavelength closest to the heated material peak absorptivity (a) or, equivalently by Kirchhoff's law ($\epsilon=a$),

closest to its peak $\varepsilon(T)$ (ex. vertical black line in Fig. 3(B)). Likewise, $\delta(\lambda_L, T)$ and reflectivity, determine the laser-material coupling efficiency, the peak steady state T , and the depth of the heat affected zone [17]. For fused silica the real refractive index, n , and reflectivity remains nearly constant with T in the IR [30, 31] unlike κ and δ . In Fig. 3(C), the linear dependence of the absorption coefficient, $1/\delta(\lambda_L, T)$ with T can be represented across a range of wavelengths by an empirical power law as determined from reported data [17, 32-34]. This T dependence of $\delta(\lambda_L, T)$ over a few hundred degrees can thus strongly affect the heating dynamics of a laser heated surface.

The accuracy of the IR-derived T measurements depends critically on the IR camera imaging wavelength, λ_p , for the following reasons. First, the emissivity at a particular wavelength may change significantly depending on the T and state of the surface (chemistry, roughness, shape, etc), although this issue may be addressed by *in situ* measurements of the emissivity [35]. Second, effectively, the IR detector will only be exposed to the thermal radiation emanating from a surface layer $\approx 3.5 \times \delta(\lambda_p, T)$ thick, representing the source for $\approx 99\%$ of all the thermal radiation emitted by the sample [27] since the thermal radiation, L_λ , is absorbed as it propagates within the bulk (Fig. 4(A)). Within this depth of $3.5 \times \delta$ the T field varies by an amount ΔT , thus the probe wavelength should be selected such that ΔT is minimized and interpretation of the the outer layer surface T is unambiguous. This is the case for fused silica at $\lambda_p = 8.9 \mu\text{m}$ where $\Delta T < 5\text{K}$ but not necessarily for other materials where ΔT can be as large as 150K (Fig. 4(B)). In those non-isothermal cases an integrated bulk T will be derived from IR imaging, which represents an apparent T that is lower than the peak outer surface T . However, this lower apparent T will tend to be more heavily weighted toward the highest outer surface T because of the exponential dependence of the emission flux (Fig. 3(A)). If a form for the axial $T(z, t)$ distribution is assumed, then a correction based on a Planck weighted emission flux can be applied to the calibration of the IR camera (section 2.3) to yield a more accurate outer surface T . Furthermore, the effect of the non-uniform axial T field will be mitigated in most cases as the sample heats up and the material becomes less transparent with T (Fig. 3(C)), as is the case for fused silica where, for example., at $\lambda = 10.6 \mu\text{m}$, $\delta(T=300\text{K}) \approx 40 \mu\text{m}$ and $\delta(T > 1000\text{K}) < 4 \mu\text{m}$.

(A)



(B)

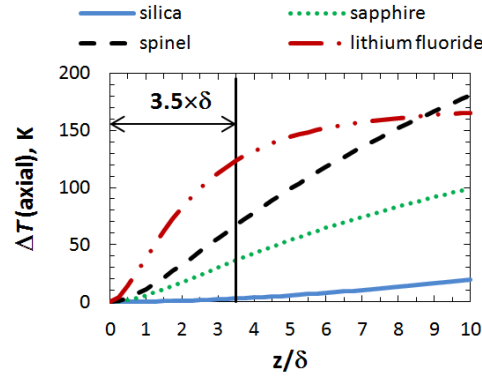


Figure 4. (A) Schematic of the laser absorption which occurs over a depth $\approx \delta(\lambda_L, T)$, with input intensity, I , at the laser wavelength, λ_L . Bulk thermal radiation, L_λ , from laser heating propagates toward the surface while being absorbed along the path, s , at a rate determined by the magnitude of δ , $\sim L_\lambda/\delta ds$. Thus, about 99% of the total radiation emitted from the surface by the laser heated material comes from a depth of about $3.5\delta(\lambda_p)$. (B) This probing depth of $3.5\delta(\lambda_p)$ is depicted by the arrow and depends on the probe wavelength and T (Fig. 3(C)). Curves of the calculated steady state axial T gradient, ΔT , are indicated for selected materials. At steady state, the calculated peak temperature and the axial T profile depend on δ , amount of reflected laser light, laser power, beam size, and the thermal conductivity of the solid.

2. 3. Calibration of IR camera

The first step in obtaining T measurements from IR images is to calibrate the optical system and the camera FPA response after insuring that both the electronics and the camera have reached a steady state T , typically 1-2 hrs after turn ON and filling in of the camera dewar in LN cooled systems. Detector sensitivity is generally optimized at $\approx 77K$ and increases when lowering T [36]. Multiple blackbody calibration sources can provide known thermal fluxes with nearly blackbody emission spectra (Fig. 3(A)) or for a the wavelengths of interest [37] (e.g., extended surface, cavity source, blackbody paint, tungsten strip lamps). Based on the set T , the known thermal flux can be used to calibrate the IR collection system, which includes the entire optical path (Fig. 1). Blackbody emissions are scaled by the blackbody source emissivity, $\epsilon_{BB} \approx 1$, and Planck's equation, L_λ , integrated around the center bandpass filter wavelength, λ_p ,

$$S_{FPA} = \int_{\lambda_p - \Delta\lambda}^{\lambda_p + \Delta\lambda} \varepsilon_{BB} C_1 \left(\lambda^5 e^{C_2/\lambda T} - 1 \right)^{-1} d\lambda \quad (1)$$

which gives the linear detector response, S_{FPA} , to the spectrally integrated thermal radiant flux ($\text{W m}^{-2} \text{sr}^{-1}$). S_{FPA} is calibrated through the first and second radiation constants C_1 and C_2 to accounts for the overall transmission of the optical system and the detector sensitivity. From Eq. (1) it is apparent that the in-band thermal flux increases exponentially with T as $\sim C_1 \lambda^{-5} \exp(-C_2/\lambda T)$, making lower T measurements more difficult depending on the noise of the system. An example of a calibration fitted with Eq. (1) above is shown in Fig. 5(A) along with the T dependent fused silica emissivity, $\varepsilon(\lambda, T)$, derived from emissivity data available in the literature (Fig. 5(B)) [38]. Taken together, the information in Fig. 5 is sufficient to relate the measured counts from each pixel in the FPA to the corresponding local T of the hot surface by numerically inverting Eq. (1) for T with ε_{BB} replaced by $\varepsilon(\lambda, T)$. The results are illustrated in Fig. 2, where the raw measured count data (Fig. 2(A)) and the T converted profile are shown (Fig. 2(B)).

In the process of calibrating the IR measurement, the orientation and location of the blackbody with respect to the viewing axis of the imaging system must be carefully adjusted. A practical viewing object, such as a metallic TEM grid, can be fixed to the blackbody aperture for focusing to insure the correct location of the IR imaging plane registered to that of the exposed surface sample, and the correct orientation of the surface. In addition, typically, a two point linear normalization of the FPA pixels is performed using a “hot” (high flux) and “cold” (low flux) scene to correct for any non-uniformity stemming from pixel-to-pixel variation in sensitivity and offsets and to detect defective pixels. Because of this step, it is important to orient the blackbody correctly otherwise the apparent image of a uniform scene will appear tilted when the correction is applied.

Ideally, the calibration should span the range of experimental fluxes expected to insure detector linearity with flux (Eq. (1)). At extreme T above about 1500K this can be a problem because blackbody sources are bulky and cannot easily be set on an optical table for manipulation. Alternatives such as lamps, which are only calibrated at a few wavelengths not necessarily of interest, are limited in their viewing area. For example, conventional tungsten strip lamps have target sizes of 1.5 or 3 mm and are mostly calibrated in the optical range. The target size problem cannot be avoided because of the implausibly high currents that would be required to heat larger strips to reach radiation T near 3000K. Another possibility is to use a gold coated integrating sphere to simulate radiance T in the wavelength band required, although such possibility has yet to be attempted [39]. Fixed-point T are useful then to check when extrapolating beyond the calibration range as discussed below.

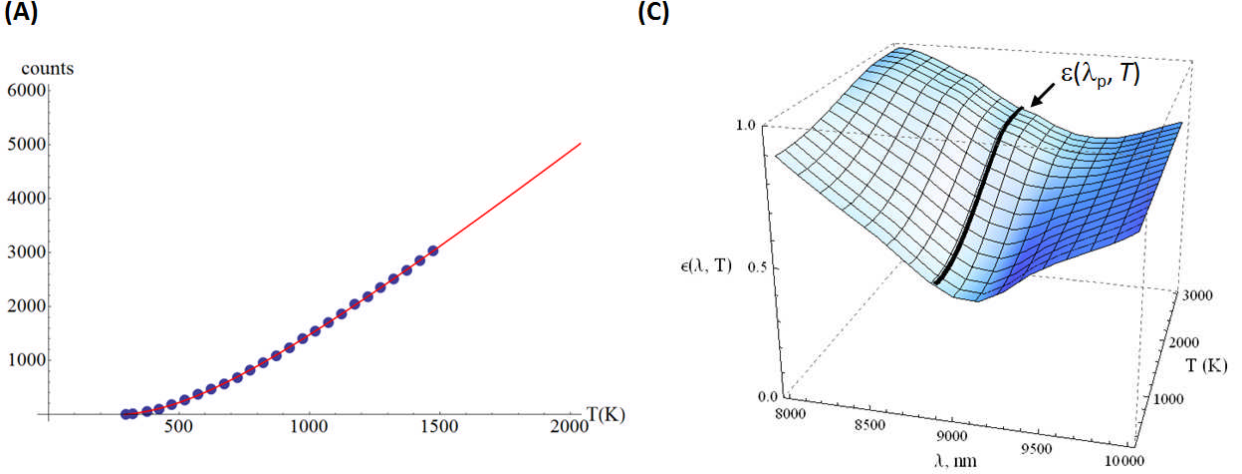


Figure 5. (A) IR optical imaging system (Fig. 1) calibration using a blackbody cavity (50-1200°C, Graseby IR Systems, FL, USA). The experimental spectral emissivity at normal viewing angle are from Ref[38].

2.4. Limitation of the IR imaging resolution and deconvolution

There are two main sources of T error inherent to T derived from IR imaging. First, the sampling depth of the thermal emission discussed in section 2.2, which can be mitigated by selecting a λ_p where the material is opaque. Second, the limited optical resolution of the imaging system, which is primarily determined by the wavelength and numerical aperture, ultimately reduces the T measurement spatial resolution. This latter source of T smearing is particularly important to consider when T varies strongly on the micrometer length scales, as is the case for a tightly focused beam. To address this problem, the point spread function (PSF) of the optical imaging system can be evaluated, allowing a deconvolution algorithm to be applied in order to retrieve the original image from the convoluted one. For example, if the laser beam profile is known, and the material properties are well described at some convenient T , one can start with a convoluted signal-PSF ‘guess’, g , where the signal is based on the calculated T and the corresponding emission profile. The laser beam profile could then be adjusted to match the convoluted signal. Alternatively, one can use the Weiner algorithm, which is conveniently included in many image or data analysis software packages (e.g. Mathematica©). Using this method, the deconvolved signal \hat{f} , can be approximated from the measured signal of the convoluted PSD and signal, f , by applying a so-called Weiner filter, h , where

$$\hat{f}(x) = h(x)[f \otimes g] \quad (2)$$

and h is constructed in frequency space using the PSD and an estimate of the measured signal-to-noise ratio. For experimental determination of the PSD function, we measured the radiant flux from a 400 μm diameter pinhole placed on top of a fused silica substrate heated with a CO_2 laser. The measured radiant flux profile was fitted to a Gaussian PSF convolved with a 400 μm step function (Fig. 6). From a best fit we find that the Gaussian PSF has a $1/e^2$ half width of 200 μm (equivalent to HWHM width of 118 μm).

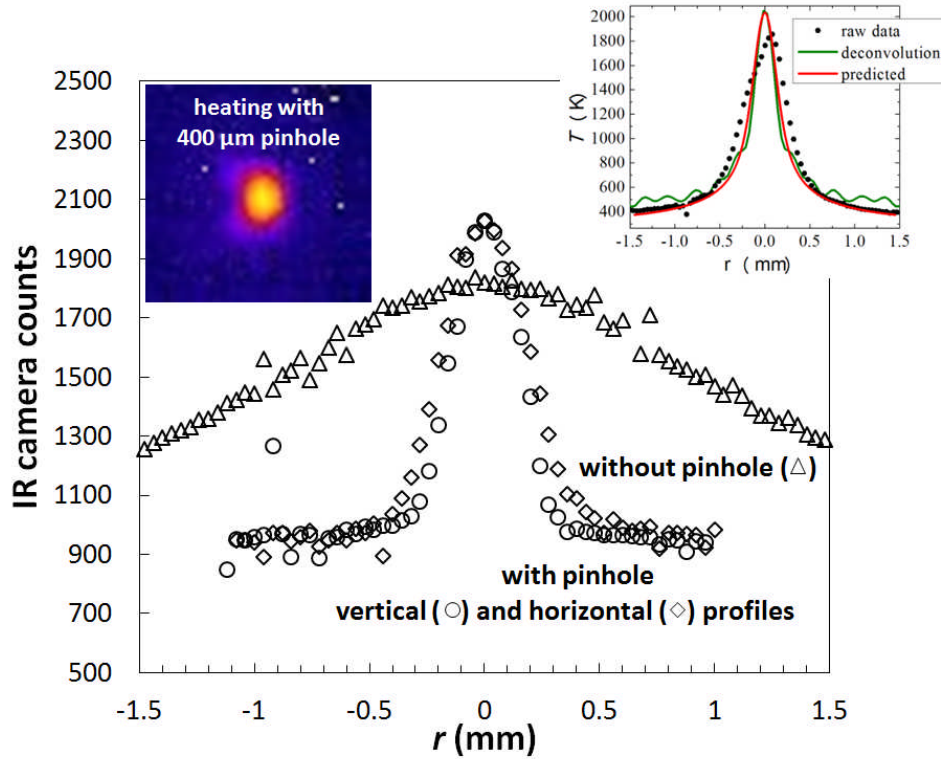


Figure 6. Example of deconvolving a measured thermal image produced by CO₂ laser heating with a 400 μm $1/e^2$ laser beam with an incident power of 1.95 W. Along with the aforementioned smearing of the diffraction limited signal, the peak axial temperature is also significantly affected. Specifically, without deconvolving the signal, an underestimate of the temperature by $\approx 200\text{K}$ might have been made. Furthermore, the deconvolved signal agrees well with the predicted profile using finite element modeling of laser-heated silica Ref[63].

2.5. Data processing

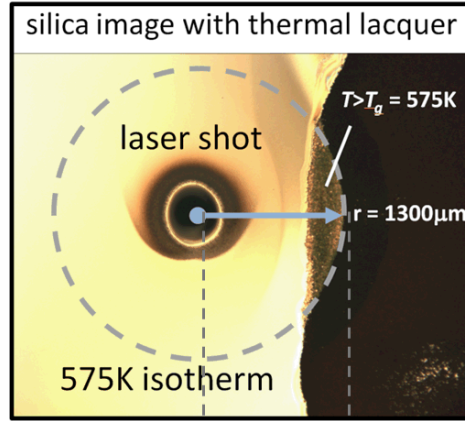
The data processing needed for analysis of IR based images and derivation of T is not unusual and can be routinely handled through commercial packages such Mathematica® or Matlab®. Typically the first few IR frames are captured before laser exposure and used as the reference frames to subtract all subsequent frames. Data handling of outliers (drop outs, etc.) can be done, for e.g., by thresholding and converting the outliers or bad pixels into NaN data type, then applying a soft median filtering to remove the noise if necessary. Over extended use of the camera (\approx hours), a drift in the baseline noise of the detector system can occur. If the viewing area is large enough that some areas are not affected by the heat significantly, then a portion of those cold areas can be used to subtract the drift from each pixel count. Batch processing of the data becomes much easier to handle without noise and to determine peak counts and T associated with each frame. For the purpose of inverting the camera counts to T , the calibrated Eq. (1) with $\varepsilon(\lambda, T)$ can be used to obtain the T for each pixel in the IR image array. For data acquisition systems with smaller bit depths, the dynamic range might be limited. Therefore, care must be taken to set the camera integration time so as to avoid saturation or to insure that low level signals are captured. The linearity of the measured counts against integration time must be determined with a

blackbody source for instance, so that the proper correction factor can be applied to the calibration curve [40].

2.6. A validation of the IR-based temperature measurements

Finally, the calibrated system should be validated using known standards or fixed-points. Material phase transitions are easily discernible and well characterized and, when applicable, should be used to test the IR imaging system representation of T and the system accuracy. In the example below a thermal lacquer paint (OMEGALAQ®-0575) was applied nearby where a silica surface was heated with CO₂ laser beam (Fig. 7(A)). A uniform thin film was smeared and dried on the working surface before the heating began. When a steady T is reached a boundary forms and stops advancing corresponding to a sharp liquid-melt crystallization transition. The melted coating does not revert to its original dull-opaque appearance but remains glossy-transparent which makes subsequent delineation of the T isotherm simple. This method is illustrated in Fig. 7(A) with a 575K rated lacquer used to find the location of the $T = 575K$ isotherm, which was then compared with the IR camera-based T profile Fig. 7(B). The lacquer did not appear to interfere with the IR measurement, and was far enough from the heated spot that light incident from the Gaussian beam was negligible.

(A)



(B)

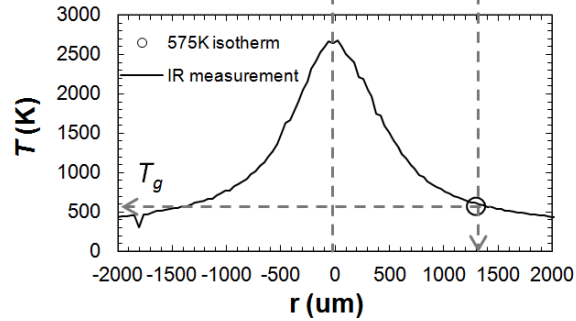


Figure 7. (A) Image of a calibrated thermal lacquer rated at 575K after undergoing a first order phase transition for temperatures above its glass transition temperature (T_g). The surface was heated by a nearby exposure with a CO_2 laser ($\sigma = 350 \mu\text{m}$) producing a melted and evaporated pit with dark re-condensed silica material. The pristine surface appears yellow in the image, and the unaffected thermal lacquer ($T < T_g$) remains dark to the right of the image. (B) The isotherm from the lacquer melt boundary was compared to the temperature profile derived from the IR imaging system in Fig. 1.

3. Thermal modeling and properties

3.1. Applicable thermal models

For many laser-induced processes, modeling of the material transformation requires the heating conditions as input. The thermal model starts with the heat flow equation below (Eq. (3)). Using laser beam coupling with an isotropic homogenous material, the following equation can be solved to obtain the T distribution $T(r, z, t)$ at the surface and within the bulk,

$$\rho C_p \frac{\partial T}{\partial t} - k \nabla^2 T = Q \quad (3)$$

for conditions where Fourier heat conduction applies [41, 42]. In Eq. (3) Q is the volumetric heating term from the laser input, ρ is the fused silica density, C_p is the specific heat, and k is the thermal

conductivity. For a Gaussian beam, with absorption depth, δ , along the z direction and $1/e$ beam radius, a , the heat source is given by,

$$Q(r, z) = \frac{I}{\delta} \exp\left(-\frac{z}{\delta}\right) \exp\left[-\left(\frac{r}{a}\right)^2\right] \quad (4)$$

while absorbed the laser intensity given by,

$$I = \frac{(1-R)P}{\pi a^2} \quad (5)$$

where R is the surface reflectivity ($R=0.15$ for fused silica [43, 44]) and P is the average laser power. The laser coupling efficiency expressed in δ and R , and the energy transfer processes will depend on pulse width and repetition frequency, based on specific absorption mechanisms that are strongly dependent on the laser temporal modes (continuous wave (CW) vs. ultrashort pulse exposures for example). Therefore, the thermal model applied should reflect the physics for the particular laser heating time regime [11, 45]. Below we address the better understood continuous wave laser heating model as an example, where near steady state heating prevails (after ≈ 1 sec exposure) and the absorbed laser intensity is nearly balanced by the heat-transfer processes.

The full heat transport Eq. (3) can be solved numerically (e.g. continuum simulations) taking into account T dependent material properties, and applying boundary conditions for radiative heat loss and surface heat loss through convection. This non-linear approach, however, is computationally intensive and does not readily yield physical insights into laser energy deposition and transport processes. An alternate approach is to neglect radiative and surface heat loss and to assume that the thermal properties are constant over the T range of interest. We will address the validity of these assumptions later to extract meaningful comparisons with T data obtained by IR imaging. Thus, using this linear diffusive approximation, the axisymmetric heat equation can be solved numerically using the Green's function method [46] to express T as a closed form integral equation [17, 18, 47-49]. However, in the limit that surface absorption is large (i.e., $a/\delta \rightarrow \infty$), most of the heat is absorbed at the surface and it can be shown that the steady state axial T reduces to,

$$T(r=0, z, t \rightarrow \infty) = \frac{(1-R)P}{2k\sqrt{\pi}a} \left(1 - e^{-\left(\frac{z}{\delta}\right)}\right) \exp\left(-\left(\frac{r}{a}\right)^2\right) + T_0 \quad (6)$$

and for the axial peak surface T becomes,

$$T(r=0, z=0, t \rightarrow \infty) = \frac{(1-R)P}{2k\sqrt{\pi}a} + T_0 \quad (7)$$

Equations (6) and (7) predict that the axial T is linear with P , and inversely with k and a . Thus a plot of T versus P/a should be linear and all data should fall on a single line if the assumptions noted above are correct and k remains constant over the T range considered. From Fig. 8 with $10.6 \mu\text{m}$ laser heating, that is indeed the case up to the power levels where evaporation starts to contribute significantly to the

cooling of the surface near silica boiling point ($\approx 2800\text{K}$ [50]). The calculated T , based on a published $k \approx 2\text{ Wm}^{-1}\text{K}^{-1}$ [51] and Eq. (7) is shown as a dashed line. These lines accurately represent the data up to the evaporation point, and the apparent linearity is consistent with the form of Eq. (6, 7). Furthermore, the assumptions that radiation transport and heat convection are not important cooling processes for this type of laser heating appears reasonable given the accuracy of the predictions in Fig. 8, which do not account for these heat dissipative mechanisms. A separate simulation study of the non-linear heat equation with radiation transport for laser heated surfaces confirms that radiation represents $<5\%$ of the total heat transfer ($\lambda_L=10.6\text{ }\mu\text{m}$, $a = 350\text{ }\mu\text{m}$, $t_{\text{exp}} = 5\text{ sec}$), and only affects the T by a few K inside the bulk [21]. For T above the boiling point, significant cooling occurs by evaporation relative to the laser heating and heat conduction fluxes. This effect is apparent in the sub-linear T dependence in Fig. 8, although some of that effect may be due to changes in the surface emissivity and reflectivity during phase transformation [52]. Thus, for the $10.6\text{ }\mu\text{m}$ laser heating case, we find that heat transport is dominated by conduction for $T < 2800\text{K}$ and is significantly altered at evaporation T above 2800K . Other heat dissipation mechanisms such as radiation and convection cooling can in general be neglected in modeling the heating of the surface at these T . To extend the range of the thermal modeling, the evaporative cooling could in principle be included in Eq. (3) as a surface boundary condition [53], especially if the evaporation kinetics are measured, as was done recently for laser heated silica [28].

In contrast with the $10.6\text{ }\mu\text{m}$ laser, $4.6\text{ }\mu\text{m}$ laser heating in studies of deep annealing [17] produced a non-linear dependence on P well below the evaporation point, and the data did not fall on a single curve (Fig. 8). Since k is constant for silica over that range of T , as established above, and the T remained below evaporation, there must be another source for the apparent non-linearity. We find a possible cause for the nonlinear heating at $4.6\text{ }\mu\text{m}$ as arising from differences in the optical constants of silica, specifically, in the laser absorption at $4.6\text{ }\mu\text{m}$ compared to $10.6\text{ }\mu\text{m}$. At $\lambda_L=4.6\text{ }\mu\text{m}$ $\delta \approx 10^3\text{ }\mu\text{m}$ compared to the much smaller absorption depth $\delta \approx 10\text{ }\mu\text{m}$ at $\lambda_L=10.6\text{ }\mu\text{m}$ (Fig. 3(B)). Under these conditions the volumetric heating in Eq. (3) cannot be approximated by surface absorption and the solutions Eq. (6) and (7) do not apply. In this semi-transparent absorption regime, a and δ become comparable even if the decrease in δ with T is included (Fig. 3(C)). For the $10.6\text{ }\mu\text{m}$ laser such reduction in δ had a negligible effect on the nature of the surface absorption since absorption is already very shallow relative to the beam size at all T . Therefore the T dependent non-linear form of Eq. (3) must now be solved numerically based on $\delta(4.6\text{ }\mu\text{m}, T)$ and a fixed k , as detailed previously [17]. The results are shown as solid curves in Fig. 8, which describes the T data well for $4.6\text{ }\mu\text{m}$ laser irradiation.

On the other hand, for materials with a T dependent $k(T)$ and constant δ (or large a/δ), a steady state solution in closed form [49] does exist avoiding the need for numerical simulations. The resulting form of the T solution can then be conveniently used to derive $k(T)$ experimentally from the IR based measurements of the peak surface T . This method was applied to laser heated sapphire, lithium fluoride, spinel, and fused silica to derive $k(T)$ up to the failure T of these materials (ex. surface cracking and oxidation). The laser λ_L was selected where those materials absorbed strongly for the reasons stated above. Therefore, the particular thermal model to be used for analysis of laser heating must include all significant heat transport mechanisms which, in turn, dependent on the specific material thermal properties and the nature of the laser-matter coupling.

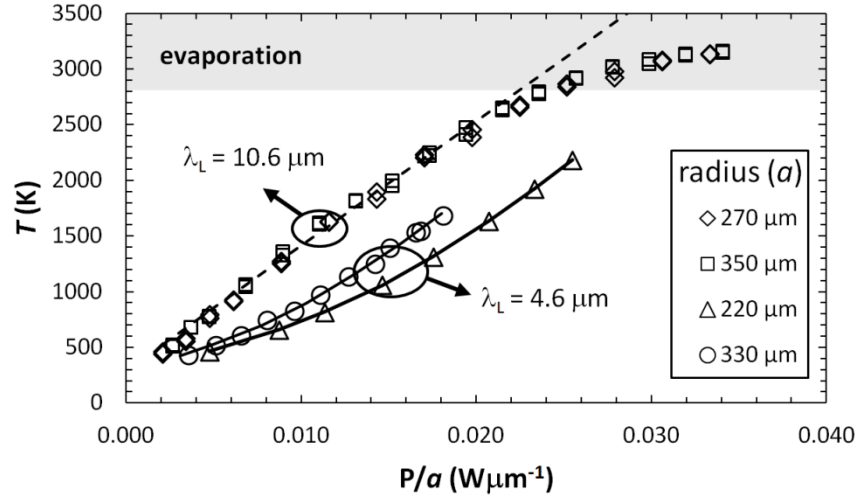


Figure 8. Experimental surface axial temperature derived from IR-imaging for fused silica heated using a 10.6 μm and a 4.6 μm CO_2 laser as indicated by the circles with arrows ($t_{\text{exp}} = 5$ sec). The data is for the beam radii, a , plotted over the normalized axis using the laser power, P , and the $1/e$ radii. The evaporation regime is delineated by the grayed area while calculated T for 4.6 μm laser are depicted by solid curves, and calculated T are shown as dashed lines for the 10.6 μm laser heating case.

3.2. Derivation of heat transport properties from IR-based temperature measurements

Once the laser heating process is well understood and its limits determined, the applicable model can be used to derive the thermophysical properties of the material tested. Using the time dependent $T(r, z, t)$ from Green's function solution to Eq. (3) described elsewhere [18], time-resolved T data (Fig. 9(A)) from IR imaging allowed determination of fused silica thermal diffusivity, D (Fig. 9(B)). Over the T range addressed, the D appears constant $\approx 8 \times 10^{-8} \text{ m}^2/\text{sec}$ unlike what is typically reported for silica D (solid and dashed curves in Fig. 9(B)). The reason for this discrepancy is as follows. With focused laser heating, the spatial T gradients are much larger than those found in measurements from conventional bulk methods. The consequence is that the steep laser T gradients drive up the thermal conduction contribution making conduction the dominant heat transport mechanisms, while making contribution from other heat transport mechanisms negligible. Hence, a simpler and more accurate heat conduction model can be applied to extract the intrinsic (phonon) D from a fit of the laser T data [47] unlike the non-laser heating cases. With measurement methods where shallower T gradients exist (surface resistive heating across a sample of finite thickness for e.g.), other heat transport mechanisms such as radiation transport or heat convection can significantly affect the experimental T . Unless these added mechanisms are properly accounted for in the thermal model -and radiation transport is difficult to model- then artificial T dependencies can arise. This situation is apparent in Fig. 9(B) where an increase in D with T usually appears to scale as a power law $\propto T^n$, mostly from radiation transport contribution. Such artifacts have been noted before in the measurement of the thermal conductivity for e.g [54, 55] but do not represent intrinsic thermal properties of the material, and are likely to be occurring for the reported measurements of D shown in Fig 9(B). In this regard, the method of using a laser beam for heating surfaces and determining thermal conductivity from T measurements tends to provide more accurate results than typical measurements.

Determination of the k for fused silica is also possible using a simple steady state solution (Eq. (7)) combined with T measurements such as those at the end of the laser exposures in Fig. 9(A). Again, the $k \approx 2 \text{ Wm}^{-1}\text{K}^{-1}$ appears constant, until it takes off when the evaporation cools the surface. The reasons for this increase are apparent from examination of Eq. (7) used to model the T with $\sim 1/k$ dependence. Any drop in the laser power dependence of the T , as was the case for the high T sub-linear evaporative region in Fig. 8, would make it appear as if the thermal conductivity increases with T . Thus evaporation needs to be included in the model to extract the intrinsic k (evaporation is not included in analysis of data in Fig. 9). Finally, once D and k are known, the specific heat of the material can also be determined from the relation $C_p = k/\rho D$ (Fig. 9(D)). We conclude this section by noting that for the type of analysis described so far, only the peak axial T were needed making the approach particularly simple to implement in spite of the seemingly complex T field generated by focused laser beams.

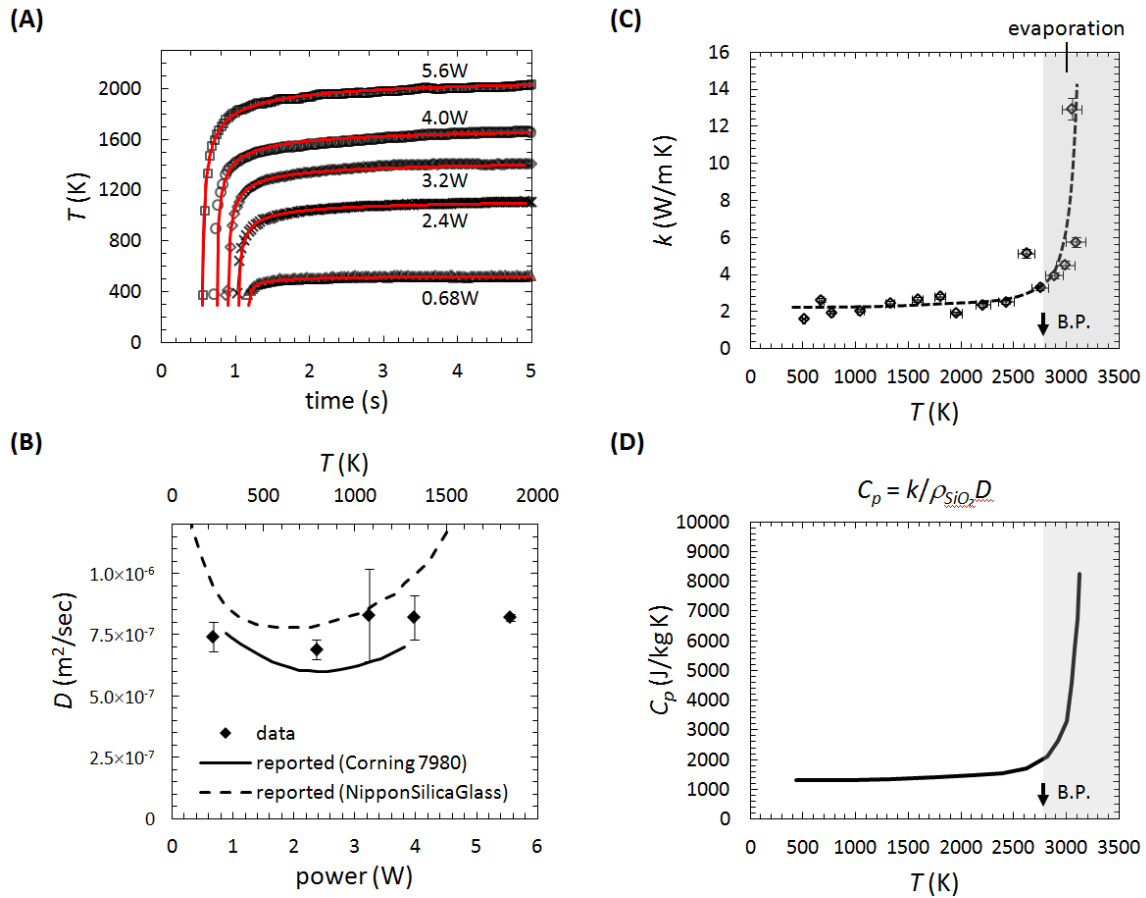


Figure 9. Derivation of the bulk thermal transport properties of fused silica using IR-imaging derived surface temperature measurements of CO_2 laser heated silica up to its boiling point (B.P.). (A) Axial surface temperature captured over a 5 sec CW laser exposure (IR camera frame rate = 33 Hz). Data were fitted (red curve) using the thermal diffusivity, D , as a free parameter in a time-dependent form of the heat flow equation solution described previously Ref[18]. The results of the fitting are shown in (B) as a function of both laser power and T and compared to reported values from sources as indicated. (C) Likewise, steady state temperatures were fitted to estimate the apparent thermal conductivity, k , of fused silica. (D) Specific heat (C_p) calculated from data in (B) and (C) through the relation shown given a fixed bulk silica density, ρ_{SiO_2} , of $2200 \text{ kg}/\text{m}^3$.

4. IR imaging of laser heated surfaces for the fundamental study of thermophysical material properties

4.1. Structural relaxation in glass

Manifestations of glassy material relaxation resulting from laser heating occurs to the extent that the material T is high enough that the relaxation times, $\tau(T)$, become comparable to the heating times resulting from laser irradiation. For glasses heated above their glass transition point, T_g , the heating produces glass-liquid transition that is reversed upon cooling to room T . For fast cooling to room T , as is often the case in laser surface heating, the molecular structure “frozen-in” reflects a fictive T_f of the material at an equilibrium T well above T_g . This higher temperature glass structure will possess fundamentally different material properties, which can affect both bulk and surface characteristics (e.g., etch rate). The gross impact of those structure modifications includes densification or volume shrinkage, a well known phenomena observed in fused silica [56]. In 10.6 μm laser heated silica surfaces densification can cause pits $\approx 0.1 \mu\text{m}$ deep and residual stresses up to 10's of MPa from structure relaxation [57-60]. An additional contribution to the stress field arises from the viscoelastic behavior, or stress relaxation, during quenching of the material (frustrated stress relaxation) which can become problematic in applications where a damage resistant flat surface is required [61].

Using infrared imaging, thermo-mechanical modeling, and *ex situ* Raman spectroscopy, the microstructural features of the laser-induced densification of fused silica were determined for a range of T up to 2100K, along with the resulting residual stress [62, 63]. In these studies, the IR-derived surface T measurements were used to validate the solution to a non-linear heating model with T dependent $k(T)$ and $\delta(T)$, which could then be used to simulate the effects of the dynamics of structural relaxation. Calculations of bulk T_f changes could then be compared with T_f based on spectral changes in the confocal Raman profiling measurements, allowing determination of relaxation parameters such as the activation enthalpy. Figure 10 below shows results of laser-induced material relaxations in fused silica for which T were measured by IR imaging (Fig. 10 (A)). It includes the pit shaping from densification, melt flow and rim formation, and evaporation, with a transitional shape from the combined material compaction ($\sim 1\text{-}2\%$) and evaporative removal apparent for the 2.25W heating case (Fig. 10(B)). The resulting residual stress from the densification and viscoelastically strained material that was unable to relax is apparent in the laser power-dependent birefringence measurements shown in Fig. 10(C). A numerical simulation using experimental T profiles as constraints can be used to relate the measured birefringence to the principal shear stress distribution in Fig. 10(D) [59, 61, 63]. Finally, the heat-affected zone where structural relaxation has occurred can be directly observed from T_f mapping derived from confocal Raman microscopy (Fig. 10(E)) and compared to Finite element model simulations using the local measured T history and a structural relaxation model [62] (Fig. 10(F)). Taken together, these results provide insights into the glass relaxation dynamics that drive the material thermo-mechanical responses important for the robustness and optical performance of laser treated materials.

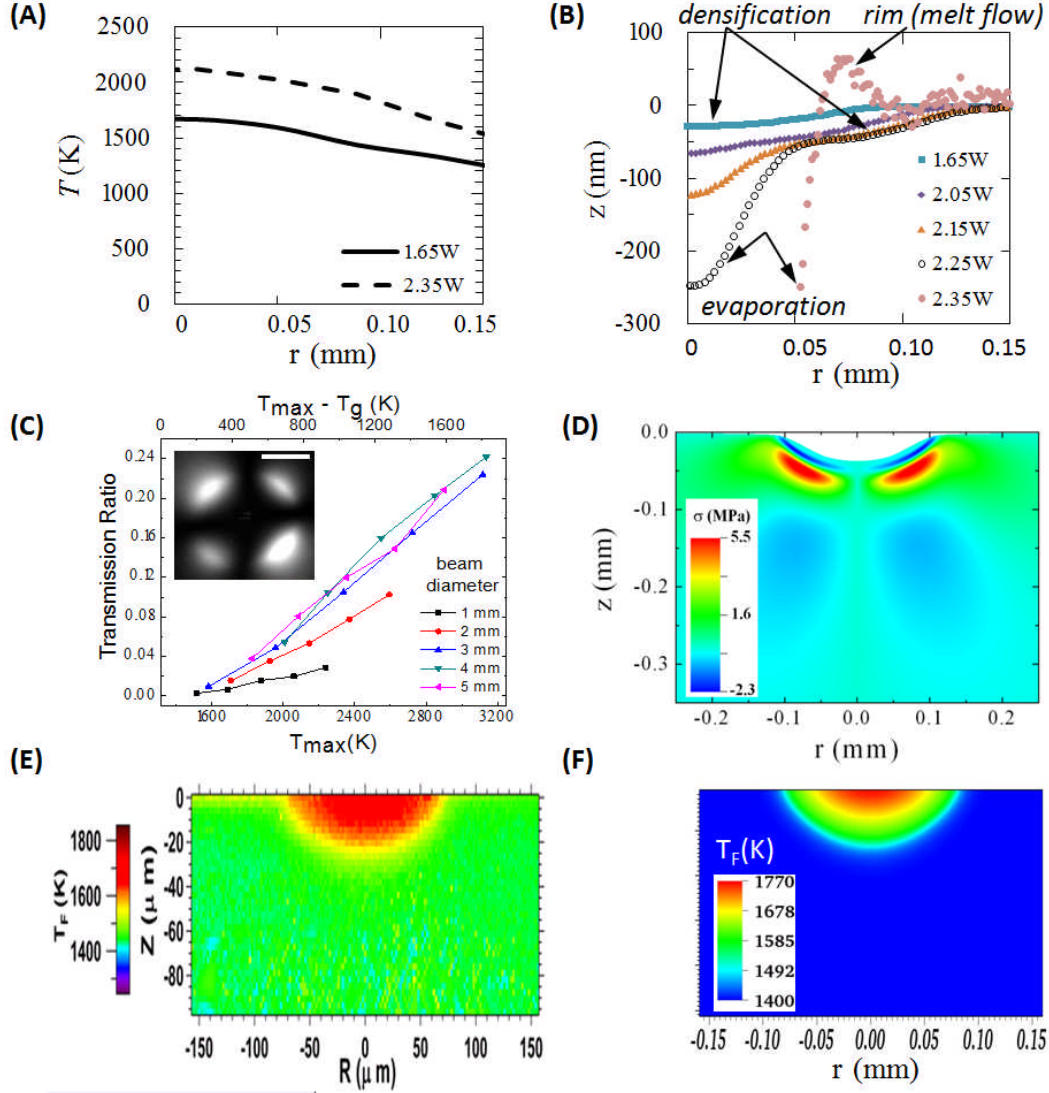


Figure 10. (A) Steady state temperature profile derived from IR imaging and (B) corresponding surface shape profiles resulting from 5 sec laser irradiation ($\lambda_L=10.6 \mu\text{m}$, $400 \mu\text{m}$ $1/e^2$ beam diameter) of a fused silica surface for the power levels indicated. The dominant pit shaping processes are indicated by the arrows with the rim produced from silica melt flow. (C) Post-laser heating birefringence measurements from linearly polarized light indicating stress areas shown in inset (white scale bar = $50 \mu\text{m}$) for the indicated $1/e^2$ beam diameters. (D) Simulated laser-induced shear stress contours from exposure at $P=1.95\text{W}$ as described elsewhere (Ref[63]). (E) Fictive temperature (T_f) measurements of a laser annealed site (experimental IR derived peak axial $T = 1670\text{K}$ for $\sim 1\text{mm}$ beam $1/e^2$ beam diameter) was measured using confocal Raman microscopy and compared to (F) predictions of T_f from a FEM numerical simulations Ref[62,17].

Another important research area for laser annealing which also used IR based T measurements, is that of defect annealing in micrometer thick SiO_2 CVD films [64] and in UV damage sites on silica optics [65, 66]. In these studies the kinetics of laser-based thermal healing of oxygen deficient centers, along with changes in defect density were determined by photoluminescence (PL) spectroscopy as a function of T and heating time. Infrared thermal imaging was applied to a moving sample during laser irradiation to characterize the T distribution and anneal conditions from CW laser irradiation (Fig. 11(A)). This stage

translation produced anneals tracks (Fig 11(B)) across which the spatial distribution of defect density was determined by PL measurements (Fig. 11(C)), which could then be registered to the T field for analysis of the defects relaxation parameters and damage threshold analysis (Fig 11(B)). The optical damage threshold [67, 68] was found to be closely related to the T driven reduction in the defects attributed to non bridging oxygen hole centers [65]. Thus, a variety of structural relaxation phenomena (Fig. 10) can easily be addressed in the high T regime of fused silica [69] and in other materials [70] by the combined laser heating-IR imaging approach. Other material properties altered by laser-induced relaxation such as junction implant annealing [71], refractive index [72], and chemical reactivity can be exploited in the fabrication of semiconductors, waveguides [73], and microfluidics [74] respectively; and could also conceivably be probed more directly using thermal imaging to more accurately assess the T driving force.

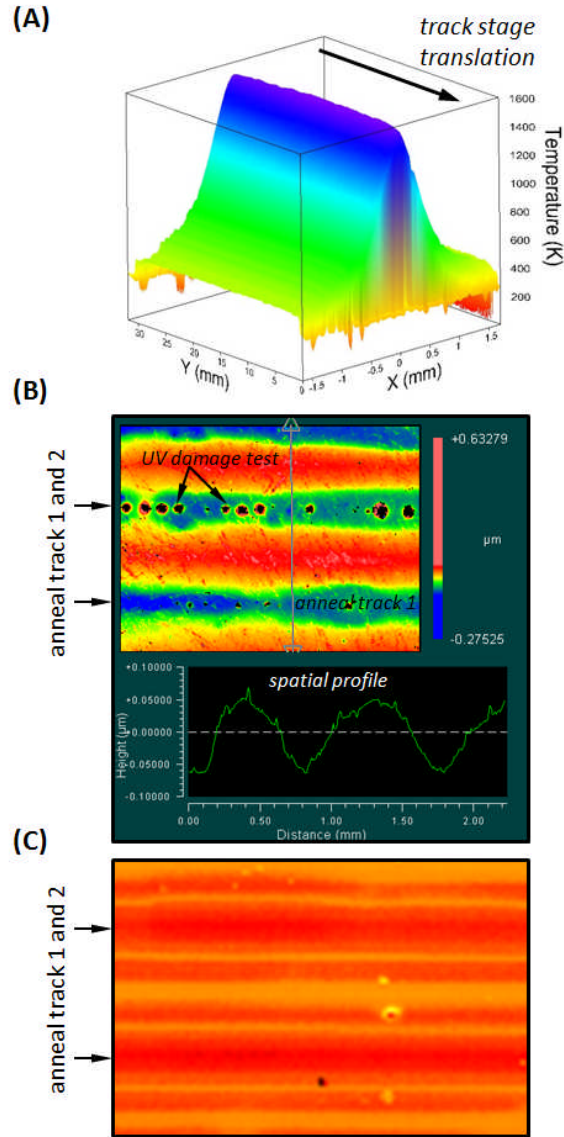


Figure. 11. (A) IR camera-derived temperature profiles along one laser anneal track produced by translating a stage with a fused silica sample exposed to a fixed CW CO₂ laser irradiation at 10.6 μm (1 mm $1/e^2$ beam diameter, $P = 3.5\text{W}$, stage speed = 50 $\mu\text{m}/\text{sec}$). (B) White light interferometry surface profile measurement of two laser anneal tracks produced at 10 and 25 $\mu\text{m}/\text{sec}$ showing a 2.5 mm section of the trenches about 0.1 μm deep. The top trench in (B) shows optical damage threshold test sites (dark spots) from 3 ns UV pulse damage testing using a series of focused shots. (B) Photoluminescence in the visible from UV light excitation of the annealed tracks as described elsewhere. A reduction in PL intensity (darker orange) indicates reduced defect density produced from laser-induced structural relaxation.

4.2. Hydrodynamics of laser induced flow

Stress relaxation by way of melt flow in laser heated surfaces is a particularly important problem to understand in laser processing technology as it determines final surface shape and finish quality. The physical processes responsible for driving the flow of the melt under laser irradiation are generally

related to the strong T gradient inherent to focused beam heating. With a radial T gradient established, both thermocapillary forces from the T dependence of the surface tension and the vaporization induced recoil pressure can drive the displacement and even ejection of the melt [75, 76] below the phase explosion regime [77]. In a recent study, IR thermal imaging was applied to probe the flow dynamics of micron-sized grating features under CW laser irradiation, where the height of the grating was reduced as the material flows by capillarity (Fig. 12). Under these conditions, the thermal input model could be decoupled from the viscous flow simulations that were used to extract the effective viscosity, $\mu(T)$, of the material based on measurement and analysis of the relaxation kinetics [78]. One interesting result, the hydroxyl (OH) content of the type III glass (1000 ppm OH) was simultaneously being reduced during heating by a thermal de-wetting process, which effectively increased the viscosity of the OH depleted silica [79] producing slower than expected flattening of the grating features. This local dewetting was further confirmed by confocal Raman spectroscopy measurements in the same study.

Likewise, rim formation dynamics in laser heated silica were recently studied as a function of laser pulse length and T , as determined by IR thermal imaging [58, 80]. The thermocapillary driven flow [81, 82] forms the indicated rim structures (Fig. 10(B)) well below the point where laser intensities can produce vapor-recoil driven flow ($>0.5 \text{ MW/cm}^2$) [76]. The magnitude of the surface rippling scaled in a complicated manner with pulse length and the type of gas atmosphere used [58]. Chemicapillary flow can be generated by a compositional gradient, such as silanol termination at the surface, from T activated surface reactions [82], although such mechanisms have yet to be demonstrated in a solid-gas phase reaction environment for the case of laser-induced surface smoothing [83]. In general, laser-induced surface smoothing has been studied with fast radiometric measurements (albeit without spatial resolution) applied to the modeling and interpretation of these processes [22, 69, 84, 85]. However, most studies still rely on 1D modeling T estimations or simply relate measurements to laser parameters [86, 87] in spite of the critical importance of T in driving material flow and the difficulty in predicting T under dynamic conditions [76].

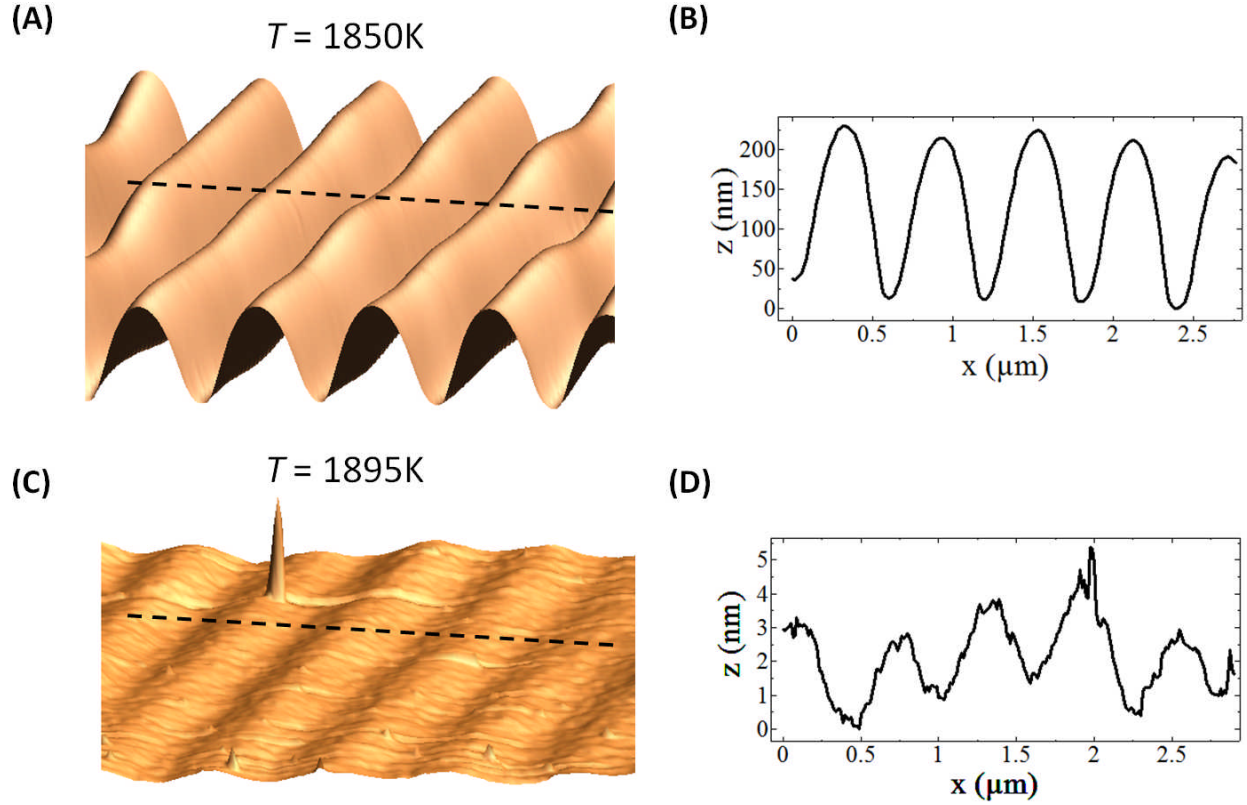


Fig. 12 AFM images of fused silica grating structure smoothed by laser-induced melt flow (100 sec exposure, $P = 3.8\text{W}$) using a CW CO_2 ($10.6\text{ }\mu\text{m}$) laser with $1\text{ mm } 1/e^2$ beam diameter. (A) Melt structure at 1850K and (B) corresponding surface profile. (C) Melt structure at 1895K and (D) corresponding surface profile. Dashed lines indicate the location of the surface profiles shown.

While laser induced material flow can produce undesirable surface rim structures, in the bulk, capillarity can have the desirable effect of healing cracks [88] that tend to increase the optical breakdown threshold of a surface [89]. Using IR thermal imaging and laser heating, an experimental comparison of crack laser healing with $4.6\text{ }\mu\text{m}$ and a $10.6\text{ }\mu\text{m}$ laser irradiation demonstrated that a $4.6\text{ }\mu\text{m}$ laser could more effectively be used to heal UV damage tracks inside the bulk (Fig. 13). As seen in the images, the cracked region progressively filled by inflowing glass leaving behind bubbles that initially grew as they coalesce but eventually disappeared when the cavities are filled. Both surface T IR measurements and fictive T measurements were used to pin the role of the absorption depth in determining the extent of the effective heat affected zone during laser driven crack healing. For $\lambda_L = 10.6\text{ }\mu\text{m}$, absorption occurs mostly at the surface (Fig. 3(B)) thus heat can only flow deep to the cracks by increasing the peak surface T and thermal diffusion, but also causing unwanted surface rippling and stress from the excess heat deposited. In contrast, with irradiation at $\lambda_L = 4.6\text{ }\mu\text{m}$, silica is more transparent and the volumetric heat generation occurs deeper in the bulk lowering peak treatment T relative to the $10.6\text{ }\mu\text{m}$ case. The IR thermal imaging approach described here allowed an unambiguous direct comparison of laser performance, particularly in cases where small differences in T produce large effects as is the case for viscous flow [90] (Fig. 12).

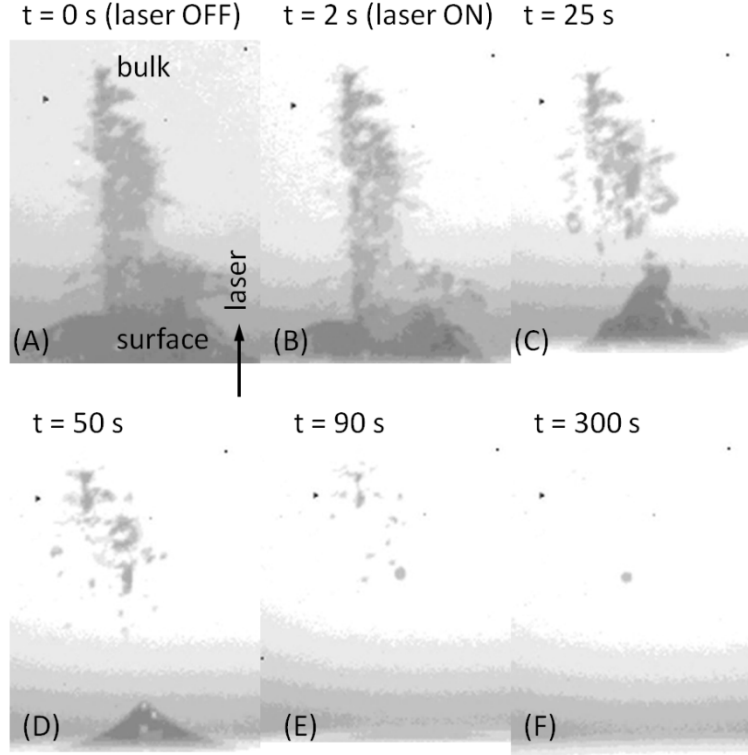


Fig. 13 (A)-(F) Laser-induced deep crack healing optical image sequence captured during $\lambda_L = 4.6 \mu\text{m}$ laser exposure of fused silica for a total of 300 sec (CW, 0.8 mm $1/e^2$ beam diameter, $P_{\text{ramp}} = 3\text{-}6\text{W}$). Temperatures during treatment were kept below 2000K as measured by surface IR thermal imaging to minimize surface rippling and evaporation. The cracked region was initially about $250 \mu\text{m}$ deep produced by UV laser irradiation above damage threshold fluence. Under similar laser healing conditions with a $\lambda_L = 10.6 \mu\text{m}$ instead, the cracked region only healed down to about $50 \mu\text{m}$ inside the bulk (not shown) due to the limited laser energy absorption at that wavelength, which increased surface T without affecting the bulk as much as in the $4.6 \mu\text{m}$ case (Ref[17]).

4.3. Solid-gas phase chemistry in laser heated materials

4.3.1. Laser-based vaporization

Above the annealing and melting T effects described above, materials start to vaporize as they get closer to their boiling point. Evaporation of the melt is an important part of the laser ablation process, which involves breaking bonds to produce volatile gas molecules by thermal decomposition, or by reaction with a reactive gas. The opposite process of condensation into a liquid phase can also take place to produce a net evaporation rate forming a pit, excluding any contribution from melt expulsion, explosive boiling, and laser damage during ultra short laser exposure for e.g [77, 91, 92]. For fused silica, a particularly tough material, the boiling point is reached for a $T \approx 3000\text{K}$ [50]. To study the evaporation chemistry at such high T under near steady laser heating, IR thermal imaging was applied to a CO_2 laser

heated silica surface exposed to neutral, reducing, and oxidizing gas flow conditions to determine the rate controlling processes; specifically, the reaction thermodynamics and mass transport [28]. The final pit volume was measured post laser treatment (Fig. 10(B)) to derive an evaporative reaction rate, $R(T)$ ($\mu\text{g}/\mu\text{m}^2/\text{sec}$), that could be related to the surface T measurement in a given gas atmosphere, or to the laser parameters through the calculated T (Eq. (3-5)). The argument was presented that the experimental evaporation rate can be estimated as $R_{\text{evap}}(r=0, z=0, T) \approx \rho d/t_{\text{exp}}$, where d is the axial pit depth, corresponding to the peak axial $T(r=0, z=0)$. Thus, for the purposes of analysis, only the peak T needed to be known and complexities related the non-uniform heating ignored.

To model the rate it can be shown that $R_{\text{evap}}(T)$ scales linearly with the equilibrium evaporation product concentration of silica in a particular gas (g_i) [93], $[SiO]_{eq}^{g_i}$, as $R_{\text{evap}}(T) = h_m [SiO]_{eq}^{g_i}$. Essentially

$[SiO]_{eq}^{g_i}$ represents the magnitude of the concentration gradient driving force across a boundary layer that is related to an evaporative flux through the kinetic mass transfer coefficient, h_m , which itself can depend on the gas properties and T . However, the significance of this result is that by taking the ratio of $R_{\text{evap}}(T)$ in different gas atmospheres the transport problem can be decoupled from the thermodynamics of the reaction by the simple relation, $R_{\text{evap}}(T, \text{pure nitrogen})/R_{\text{evap}}(T, \text{air}) \approx [SiO]_{eq}^{N_2} / [SiO]_{eq}^{\text{air}}$ since N_2 is the dominant buffer gas in both gas atmospheres with nearly the same h_m . In principle, any other gas reactant, such as H_2 in that study, can also be used to address the thermodynamics of specific evaporative reactions (Fig. 14). Thus, using this approach, the free energy of the decomposition and reduction of fused silica reactions were experimentally evaluated up to $\approx 3000\text{K}$ by fitting the data in Fig. 14. The results compared reasonably well with extrapolation from literature thermodynamical databases in the T regime where conditions for near-equilibrium are better approximated, i.e., for high evaporation rates and relatively slow mass transport. There is at least one other recent report of a high T IR thermal imaging study applied to laser evaporation in ambient air [80], albeit without the more detailed interpretation or fitting of the results given here or described elsewhere for multiphase transitions [94].

fit parameters (3000K)	ΔH°	ΔS°	ΔG_r°
$\text{SiO}_2(\text{s}) \rightleftharpoons \text{SiO}(\text{g}) + \frac{1}{2}\text{O}_2(\text{g})$	62.3	15.9	14.6
$\text{SiO}_2(\text{s}) + \text{H}_2(\text{g}) \rightleftharpoons \text{SiO}(\text{g}) + \text{H}_2\text{O}(\text{g})$	68.5	24.6	-5.4

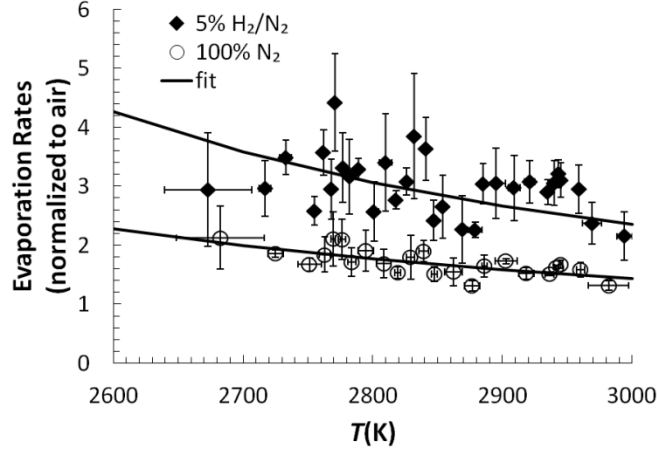


Fig. 14. Experimental evaporation rates of CO_2 laser heated fused silica in pure nitrogen (100% N_2) and in 5% H_2/N_2 atmospheres for the T measured using IR thermal imaging (Ref[28]). The beam was ≈ 1 mm in diameter ($1/\text{e}^2$) with 5 sec exposures. The data fitting (solid curves) was used with a reaction mechanism model to extract the reaction free energy of the silica decomposition and reduction with H_2 reactions. Results of the fitting for $T=3000\text{K}$ are shown in the table.

To determine the feasibility of using laser-based particle removal, the silica evaporation kinetics above were applied to a particle laser-heating model of micron-sized silica particles [95]. A Mie scattering absorption energy source term (Q) was used in the thermal model with a T dependent extinction coefficient, $\kappa(T) = \lambda / 4\pi\delta(T)$ (Fig. 3(C)). The spherical particles were deposited as a monolayer on a non-absorbing Germanium substrate and exposed to CO_2 laser irradiation at $\lambda_L = 10.6 \mu\text{m}$ for 5 seconds. The resulting spatial and temporal particle T field from IR thermal imaging was used to assign a T history to individual particles. These experimental T results were then compared to predictions of the particles T from the modified heating model [95] (Fig. 15 (A)) with reasonably good agreement considering that the evaporation kinetics used in the particle model were derived from measurements on bulk silica. Furthermore, comparison of laser heating of a monolayer of particles (Fig 15 (A)) with laser heating of a bulk silica surface (Fig 15(B)) illustrates the remarkable differences in both the time dependent T evaluation and the relatively large fluences needed to heat silica particles cooled by contact to a substrate. While for bulk laser heating the T gradually increases according to the thermal diffusion, laser heated particles on the other hand start to shrink as they are heated above their evaporation T . This produces a fast initial rise of T before shrinking has time to occur, followed by a reduction in the Mie energy absorption when the particle radius gets smaller thus producing the observed sudden reduction in T . These insights and measurements illustrate the practical nature of the combined laser-IR thermal imaging approach, which would have been very difficult to obtain by most other methods considering the length scales and high T of the problem. In general however, most laser-vaporization studies lack direct T data [53, 96, 97] and must rely on indirect measurements based on observable thermal effects to validate calculated T [77].

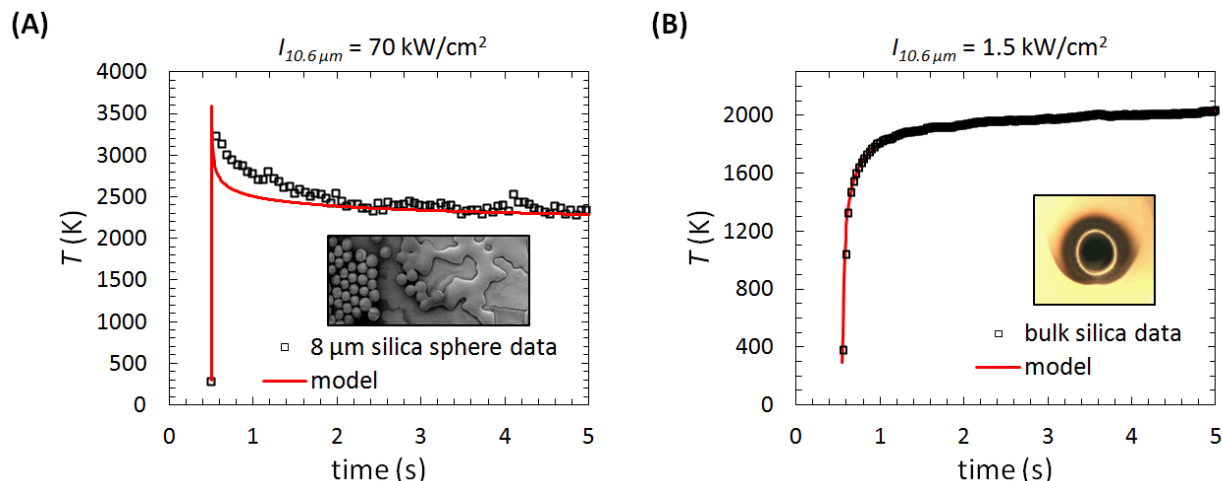


Figure 15. (A) IR thermal imaging T measurements of CO₂ laser heated silica particles ($170 \mu\text{m}$ $1/e^2$ beam diameter, 16 fps IR camera capture rate) with a model prediction based on the laser parameters and calculation of the Mie scattering absorption source term for 8 μm spherical silica particles. The inset in (A) is an SEM image after laser heating showing melted and evaporated regions of the particles monolayer. (B) IR thermal imaging T measurements of the CO₂ laser heated silica bulk surface ($1000 \mu\text{m}$ $1/e^2$ beam diameter, 33 fps IR camera capture rate) with a model description based on the solution to Eq. (3). The inset is an optical image of a typical laser heated spot (see Fig. 7).

4.3.2. Laser-based fabrication

In the previous section we discussed the removal of material from laser-based evaporative heating, in the following section we discuss the reverse process of adding material using laser-based deposition. There are a variety of laser driven processes that can deposit material on a substrate, including laser chemical vapor deposition (LCVD) [98, 99] and pulsed laser deposition (PLD). The latter process amounts to a transfer of material from a target to a substrate via a plume or gas mixture containing the material to be deposited [100]. Pyrolytic LCVD on the other hand relies on the thermal decomposition of a vapor phase precursor which can then polymerize on a substrate. Because the process is thermally driven, surface T measurements are important to understand the thermochemical and thermophysical mechanisms involved and, also, to control deposition parameters. Most T used for deposition do not exceed $\approx 1500\text{K}$ to avoid substrate deterioration and homogenous nucleation of the precursors into a powder contaminant [101]. However, to probe the very small dimensions of a focused beam LCVD reaction site, IR thermal imaging remains uniquely suited for the task of characterizing the T field during the laser deposition. Yet, very few studies have used IR thermal imaging for this purpose in laser based application [102, 103], whereas T measurements are routine for bulk chamber based CVD. In one such study of gold LCVD on gold substrate [102] T measurements were made in the configuration shown in Fig. 17, which uses a modulated signal, lock-in amplifier, a LN cooled InSb camera ($2\text{-}5 \mu\text{m}$) for IR emission radiometry, a Ar-ion laser for heating the surface, and a flow system to supply the organometallic volatile gold precursor. The emissivity in the useful band of the camera was determined by calibration with a heated stage and a thermocouple to measure the uniform sample T . As a result of

the *in situ* T measurements, an initial rise in T was uncovered that could be attributed to the exothermic decomposition reaction of the precursor, followed by a drop in T due to onset of mass transport limitations for the pressures used. In addition, growth conditions were optimized by modulating the laser input to produce smoother, crack free deposits, while IR emissivity measurements during laser annealing allowed tracking progress in surface quality. In this example, the exothermic reaction would likely have been omitted from the thermal models typically used to infer T from laser parameters [104, 105], making macroscopic observation of the deposition characteristic difficult to interpret. Thus, in general, IR thermal imaging of focused laser based processes where chemical reactions occur is particularly useful and almost required for systematic analysis and control.

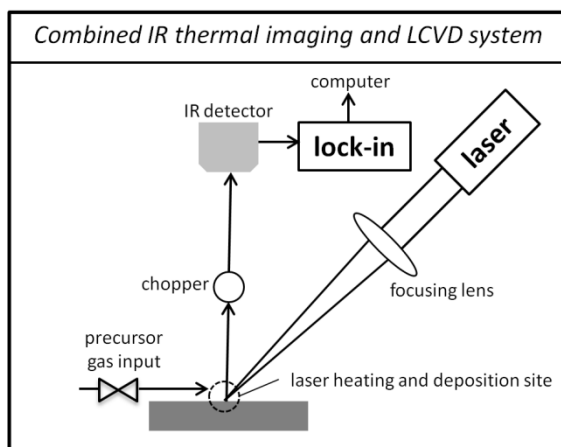


Figure 17. Experimental setup for the combined IR thermal imaging and LCVD system from Ref[102].

4. Conclusions

This review focused on the implementation and application of IR thermal imaging to laser heated surfaces as a means to effectively derive thermophysical properties under extreme temperatures. A combined pump (laser heating)-probe (IR imaging) approach is particularly well suited for these type of applications as discussed in this review. In general, we observe in the literature that temperature measurements are lacking in laser heating applications where they would be necessary for proper interpretation of the macroscopic manifestation of laser-induced effects. Instead, model based temperatures are used to characterize the driving force based on laser parameters and extrapolated material properties. However, for all but the simplest cases, the thermal model itself needs to be validated because of the complexity involved with defining all the relevant heat transfer mechanisms that occur during intense laser irradiation. The likely reason for missing IR derived T is the apparent difficulty in implementing radiometric measurements that are meaningful and well calibrated. We discussed here one specific IR thermal imaging implementation in laser heating system that can probe a broad range of fundamental thermal properties, but requires careful examination of the relevant thermal model. Such examination almost certainly means understanding laser-matter coupling processes and the emissive properties of the surface for accurate assessments to be made. The difficulty in determining emissivity under dynamic conditions along with the availability of practical calibration sources above $\approx 2000\text{K}$ remain the limiting factor in applying more broadly the approach

described, even when it's necessary. The benefits in getting beyond current experimental T limitations however are clear from the result of studies which operate with an experimental model system at the intersection of laser heating and IR thermal imaging.

Acknowledgments

The authors would like to thank the following for contributing to the studies reviewed here, Dr. Nan Shen, Dr. Ted Laurence, Dr. Rajesh Raman, Dr. Isaac Bass, Gabe Guss, and Dr. Jeff Bude for useful discussions on silica IR emissivity measurements. This work performed under the auspices of the U.S. Department of Energy by Lawrence Livermore National Laboratory under Contract DE-AC52-07NA27344.

References

1. J.D. Majumdar, I. Manna, "Laser material processing," *International Materials Reviews*, vol. 56, no. 5-6, pp. 341-388, 2011.
2. M. Balkanski, "Fundamentals of laser annealing," Springer-Verlag, New York, 1984, pp. 2-13.
3. A.C. Tam, W.P. Leung, W. Zapka, W. Ziemlich, "Laser-Cleaning Techniques for Removal of Surface Particulates," *Journal of Applied Physics*, vol. 71, no. 7, pp. 3515-3523, 1992.
4. J.J. Gonzalez, C. Liu, S.B. Wen, X. Mao, R.E. Russo, "Glass particles produced by laser ablation for ICP-MS measurements," *Talanta*, vol. 73, no. 3, pp. 577-582, 2007.
5. B. Fernandez, F. Claverie, C. Pecheyran, O.F.X. Donard, "Direct analysis of solid samples by fs-LA-ICP-MS," *Trac-Trends in Analytical Chemistry*, vol. 26, no. 10, pp. 951-966, 2007.
6. S.G. Park, K.K. Murray, "Infrared Laser Ablation Sample Transfer for MALDI Imaging," *Analytical Chemistry*, vol. 84, no. 7, pp. 3240-3245, 2012.
7. J.F. McGilp, "A review of optical second-harmonic and sum-frequency generation at surfaces and interfaces," *Journal of Physics D-Applied Physics*, vol. 29, no. 7, pp. 1812-1821, 1996.
8. S.M. Huang, M.H. Hong, B.S. Luk'yanchuk, Y.W. Zheng, W.D. Song, Y.F. Lu, T.C. Chong, "Pulsed laser-assisted surface structuring with optical near-field enhanced effects," *Journal of Applied Physics*, vol. 92, no. 5, pp. 2495-2500, 2002.
9. T.Q. Qiu, C.L. Tien, "Short-Pulse Laser-Heating on Metals," *International Journal of Heat and Mass Transfer*, vol. 35, no. 3, pp. 719-726, 1992.
10. M.D. Perry, B.C. Stuart, P.S. Banks, M.D. Feit, V. Yanovsky, A.M. Rubenchik, "Ultrashort-pulse laser machining of dielectric materials," *Journal of Applied Physics*, vol. 85, no. 9, pp. 6803-6810, 1999.
11. Y.L. Yao, H.Q. Chen, W.W. Zhang, "Time scale effects in laser material removal: a review," *International Journal of Advanced Manufacturing Technology*, vol. 26, no. 5-6, pp. 598-608, 2005.
12. I.S. Anisimov, A.V. Khojlov, *Instabilities in Laser-Matter Interaction*. CRC, 1995.
13. A. Mermillod-Blondin, C. Mauclair, A. Rosenfeld, J. Bonse, I.V. Hertel, E. Audouard, R. Stoian, "Size correction in ultrafast laser processing of fused silica by temporal pulse shaping," *Applied Physics Letters*, vol. 93, no. 2, pp., 2008.
14. M. Spyridaki, E. Koudoumas, P. Tzanetakis, C. Fotakis, R. Stoian, A. Rosenfeld, I.V. Hertel, "Temporal pulse manipulation and ion generation in ultrafast laser ablation of silicon," *Applied Physics Letters*, vol. 83, no. 7, pp. 1474-1476, 2003.
15. S.V. Ushakov, A. Navrotsky, "Experimental Approaches to the Thermodynamics of Ceramics Above 1500 degrees C," *Journal of the American Ceramic Society*, vol. 95, no. 5, pp. 1463-1482, 2012.
16. G.R. Gathers, "Dynamic Methods for Investigating Thermo-Physical Properties of Matter at Very High-Temperatures and Pressures," *Reports on Progress in Physics*, vol. 49, no. 4, pp. 341-396, 1986.

17. S.T. Yang, M.J. Matthews, S. Elhadj, D. Cooke, G.M. Guss, V.G. Draggoo, P.J. Wegner, "Comparing the use of mid-infrared versus far-infrared lasers for mitigating damage growth on fused silica," *Applied Optics*, vol. 49, no. 14, pp. 2606-2616, 2010.
18. S.T. Yang, M.J. Matthews, S. Elhadj, V.G. Draggoo, S.E. Bisson, "Thermal transport in CO₂ laser irradiated fused silica: In situ measurements and analysis," *Journal of Applied Physics*, vol. 106, no. 10, pp. 103106, 2009.
19. W. Tian, W.K.S. Chiu, "Radiation modeling of stationary fused silica rods and fibers heated by CO₂ laser irradiation," *Numerical Heat Transfer Part a-Applications*, vol. 46, no. 2, pp. 115-130, 2004.
20. J.E. Sinko, C.R. Phipps, "Modeling CO₂ laser ablation impulse of polymers in vapor and plasma regimes," *Applied Physics Letters*, vol. 95, no., pp. 131105, 2009.
21. J. Colvin, A. Shestakov, J. Stolken, R. Vignes, "The role of radiation transport in the thermal response of semitransparent materials to localized laser heating," *Journal of Applied Physics*, vol. 109, no. 5, pp. -, 2011.
22. S.C. Chen, C.P. Grigoropoulos, "Noncontact nanosecond-time-resolution temperature measurement in excimer laser heating of Ni-P disk substrates," *Applied Physics Letters*, vol. 71, no. 22, pp. 3191-3193, 1997.
23. D. Otte, H. Kleinschmidt, O. Bostanjoglo, "Space and time resolved temperature measurements in laser pulse-produced metal melts," *Review of Scientific Instruments*, vol. 68, no. 6, pp. 2534-2537, 1997.
24. Z.M. Zhang, in: V. Prasad, Y. Jaluria, G. Chen, (Ed.)[^](Eds.)Annual Review of Heat Transfer Online; Begell House, Redding, Connecticut, 2000, p 351-411.
25. J.B. Cui, K. Amtmann, J. Ristein, L. Ley, "Noncontact temperature measurements of diamond by Raman scattering spectroscopy," *Journal of Applied Physics*, vol. 83, no. 12, pp. 7929-7933, 1998.
26. D.R.T. Zahn, "Probing surfaces and interfaces with optical techniques," *Surface Review and Letters*, vol. 1, no. 4, pp. 421-428, 1994.
27. R. Gardon, "The Emissivity of Transparent Materials," *Journal of the American Ceramic Society*, vol. 39, no. 8, pp. 278-287, 1956.
28. S. Elhadj, M.J. Matthews, S.T. Yang, D.J. Cooke, "Evaporation kinetics of laser heated silica in reactive and inert gases based on near-equilibrium dynamics," *Optics Express*, vol. 20, no. 2, pp. 1575-1587, 2012.
29. A. Rogalski, "Infrared detectors: an overview," *Infrared Physics & Technology*, vol. 43, no. 3-5, pp. 187-210, 2002.
30. C.Z. Tan, J. Arndt, "Temperature dependence of refractive index of glassy SiO₂ in the infrared wavelength range," *Journal of Physics and Chemistry of Solids*, vol. 61, no. 8, pp. 1315-1320, 2000.
31. T. Toyoda, M. Yabe, "The Temperature-Dependence of the Refractive-Indexes of Fused-Silica and Crystal Quartz," *Journal of Physics D-Applied Physics*, vol. 16, no. 5, pp. L97-L100, 1983.
32. E.C. Beder, C.D. Bass, Shacklef.WI, "Transmissivity and Absorption of Fused Quartz between 0.22 μ m and 3.5 μ m from Room Temperature to 1500 Degrees C," *Applied Optics*, vol. 10, no. 10, pp. 2263-&, 1971.
33. A.D. McLachlan, F.P. Meyer, "Temperature-Dependence of the Extinction Coefficient of Fused-Silica for Co₂-Laser Wavelengths," *Applied Optics*, vol. 26, no. 9, pp. 1728-1731, 1987.
34. I.L. Bass, S.A. Payne, G.M. Guss, P. Mak, M. Lancaster, C. Dunay, in: (Ed.)[^](Eds.), Livermore, 2005.
35. D. Basak, U.R. Kattner, J.L. McClure, D. Josell, A. Cezairliyan, "Application of laser polarimetry to the measurement of specific heat capacity and enthalpy of the alloy 53Nb-47Ti (mass %) in the temperature range 1600 to 2000 K by a millisecond-resolution pulse heating technique," *International Journal of Thermophysics*, vol. 21, no. 4, pp. 913-926, 2000.
36. D.W. Goodwin, "Cooled Photoconductive Detectors Using Indium Antimonide," *Journal of Scientific Instruments*, vol. 34, no. 9, pp. 367-368, 1957.

37. A.V. Murthy, B.K. Tsai, R.D. Saunders, "Radiative calibration of heat-flux sensors at NIST: Facilities and techniques," *Journal of Research of the National Institute of Standards and Technology*, vol. 105, no. 2, pp. 293-305, 2000.
38. O. Rozenbaum, D.D. Meneses, Y. Auger, S. Chermanne, P. Echegut, "A spectroscopic method to measure the spectral emissivity of semi-transparent materials up to high temperature," *Review of Scientific Instruments*, vol. 70, no. 10, pp. 4020-4025, 1999.
39. M. Prof. Graham, in: (Ed.)[^](Eds.), 2008.
40. A.W. Jackson, A.C. Gossard, "Thermal imaging of wafer temperature in MBE using a digital camera," *Journal of Crystal Growth*, vol. 301, no., pp. 105-108, 2007.
41. R.E. Harrington, "Application of Theory of Heat Conduction to Absorption of Blackbody Radiation," *Journal of Applied Physics*, vol. 38, no. 8, pp. 3266-3270, 1967.
42. R.E. Harrington, "Thermal Conduction near a Metal Surface Exposed to Blackbody Radiation," *Journal of Applied Physics*, vol. 39, no. 8, pp. 3699, 1968.
43. R. Kitamura, L. Pilon, M. Jonasz, "Optical constants of silica glass from extreme ultraviolet to far infrared at near room temperature," *Applied Optics*, vol. 46, no. 33, pp. 8118-8133, 2007.
44. P. Bouchut, D. Decruppe, L. Delrive, "Fused silica thermal conductivity dispersion at high temperature," *Journal of Applied Physics*, vol. 96, no. 6, pp. 3221-3227, 2004.
45. A.P. Mackwood, R.C. Crafer, "Thermal modelling of laser welding and related processes: a literature review," *Optics and Laser Technology*, vol. 37, no. 2, pp. 99-115, 2005.
46. H.S. Carslaw, J.C. Jaeger, *Conduction of Heat in Solids*. 2nd ed., OXFORD university press, Great Clarendon, 2000.
47. S. Elhadj, M.J. Matthews, S.T. Yang, D.J. Cooke, J.S. Stolken, R.M. Vignes, V.G. Draggoo, S.E. Bisson, "Determination of the intrinsic temperature dependent thermal conductivity from analysis of surface temperature of laser irradiated materials," *Applied Physics Letters*, vol. 96, no. 7, pp. 071110, 2010.
48. M. Lax, "Temperature Rise Induced by a Laser-Beam," *Journal of Applied Physics*, vol. 48, no. 9, pp. 3919-3924, 1977.
49. M. Lax, "Temperature Rise Induced by a Laser-Beam .2. Non-Linear Case," *Applied Physics Letters*, vol. 33, no. 8, pp. 786-788, 1978.
50. H.L. Schick, "A Thermodynamic Analysis of the High-Temperature Vaporization Properties of Silica," *Chemical Reviews*, vol. 60, no. 4, pp. 331-362, 1960.
51. H.T. Smyth, H.S. Skogen, W.B. Harsell, "Thermal Capacity of Vitreous Silica," *Journal of the American Ceramic Society*, vol. 36, no. 10, pp. 327-328, 1953.
52. G.A. Kobzev, V.A. Petrov, "Behavior of Thermal-Radiation Properties of Oxide Ceramics under Subsecond Laser-Heating," *International Journal of Thermophysics*, vol. 14, no. 3, pp. 371-381, 1993.
53. S.R. Franklin, R.K. Thareja, "Simplified model to account for dependence of ablation parameters on temperature and phase of the ablated material," *Applied Surface Science*, vol. 222, no. 1-4, pp. 293-306, 2004.
54. H. Charnock, "Experimental and Theoretical Comparison of Radiation Conductivity Predicted by Steady-State Theory with That Effective under Periodic Temperature Conditions," *Journal of the American Ceramic Society*, vol. 44, no. 7, pp. 313-317, 1961.
55. W.D. Kingery, "Heat-Conductivity Processes in Glass," *Journal of the American Ceramic Society*, vol. 44, no. 7, pp. 302-304, 1961.
56. R. Bruckner, "Properties and structure of vitreous silica. I," *Journal of Non-Crystalline Solids*, vol. 5, no., pp. 123-175, 1970.

57. W. Dai, X. Xiang, Y. Jiang, H.J. Wang, X.B. Li, X.D. Yuan, W.G. Zheng, H.B. Lv, X.T. Zu, "Surface evolution and laser damage resistance of CO₂ laser irradiated area of fused silica," *Optics and Lasers in Engineering*, vol. 49, no. 2, pp. 273-280, 2011.
58. S. Elhadj, M.J. Matthews, G.M. Guss, I.L. Bass, "Laser-based dynamic evaporation and surface shaping of fused silica with assist gases: a path to rimless laser machining," *Applied Physics B: Lasers and Optics*, (in print).
59. M.D. Feit, M.J. Matthews, T.F. Soules, J.S. Stolken, R.M. Vignes, S.T. Yang, J.D. Cooke, "Densification and residual stress induced by CO₂ laser-based mitigation of SiO₂ surfaces," *Laser-Induced Damage in Optical Materials: 2010*, vol. 7842, no., pp., 2010.
60. C.M. Liu, Y. Jiang, C.S. Luo, X.Y. Shi, W. Ren, X. Xiang, H.J. Wang, S.B. He, X.D. Yuan, H.B. Lv, W.G. Zheng, X.T. Zu, "The Structure Evolution of Fused Silica Induced by CO₂ Laser Irradiation," *Chinese Physics Letters*, vol. 29, no. 4, pp., 2012.
61. J.J. Adams, M. Bolourchi, J.D. Bude, G.M. Guss, M.J. Matthews, M.C. Nostrand, "Results of applying a non-evaporative mitigation technique to laser-initiated surface damage on fused-silica," *Laser-Induced Damage in Optical Materials: 2010*, vol. 7842, no., pp., 2010.
62. M.J. Matthews, R.M. Vignes, D. Cooke, S.T. Yang, J.S. Stolken, "Analysis of microstructural relaxation phenomena in laser-modified fused silica using confocal Raman microscopy," *Optics Letters*, vol. 35, no. 9, pp. 1311-1313, 2010.
63. R.M. Vignes, T.F. Soules, J.S. Stolken, R.R. Settgast, S. Elhadj, M.J. Matthews, "Thermo-mechanical modeling of laser-induced structural relaxation and deformation of SiO₂ glass," *Journal of the American Ceramic Society*, (in print).
64. N. Shen, M.J. Matthews, S. Elhadj, P. Miller, A. Nelson, J. Hamilton, "Correlating optical damage threshold with intrinsic defect populations in fused silica as a function of heat treatment temperature," (submitted).
65. R.N. Raman, M.J. Matthews, J.J. Adams, S.G. Demos, "Monitoring annealing via CO₂ laser heating of defect populations on fused silica surfaces using photoluminescence microscopy," *Optics Express*, vol. 18, no. 14, pp. 15207-15215, 2010.
66. R.N. Raman, M.J. Matthews, S. Elhadj, N. Shen, L.D. Flores, "Microstructural relaxation dynamics under CO₂ laser annealing of laser-modified fused silica," (submitted), vol., no., pp., 2012.
67. A.E. Chmel, "Cumulative effect in laser-induced damage of optical glasses: A review," *Glass Physics and Chemistry*, vol. 26, no. 1, pp. 49-58, 2000.
68. C.W. Carr, J.D. Bude, P. DeMange, "Laser-supported solid-state absorption fronts in silica," *Physical Review B*, vol. 82, no. 18, pp. 184304, 2010.
69. L. Li, T.D. Bennett, "Incandescence measurement during CO₂ laser texturing of silicate glass," *Journal of Heat Transfer-Transactions of the Asme*, vol. 123, no. 2, pp. 376-381, 2001.
70. Y. Shin, Y. Kim, S. Park, B. Jung, J. Lee, J.S. Nelson, "Pit and rim formation during laser marking of acrylonitrile butadiene styrene plastic," *Journal of Laser Applications*, vol. 17, no. 4, pp. 243-246, 2005.
71. B. Adams, A. Mayur, A. Hunter, R. Ramanujam, "Pyrometry for laser annealing," *13th IEEE International Conference on Advanced Thermal Processing of Semiconductors - RTP 2005*, vol., no., pp. 105-109, 2005.
72. H. Kakiuchida, K. Saito, A.J. Ikushima, "Refractive index, density and polarizability of silica glass with various fictive temperatures," *Japanese Journal of Applied Physics Part 2-Letters & Express Letters*, vol. 43, no. 6A, pp. L743-L745, 2004.
73. K.M. Davis, K. Miura, N. Sugimoto, K. Hirao, "Writing waveguides in glass with a femtosecond laser," *Optics Letters*, vol. 21, no. 21, pp. 1729-1731, 1996.

74. A. Marcinkevicius, S. Juodkazis, M. Watanabe, M. Miwa, S. Matsuo, H. Misawa, J. Nishii, "Femtosecond laser-assisted three-dimensional microfabrication in silica," *Optics Letters*, vol. 26, no. 5, pp. 277-279, 2001.
75. V. Semak, A. Matsunawa, "The role of recoil pressure in energy balance during laser materials processing," *Journal of Physics D-Applied Physics*, vol. 30, no. 18, pp. 2541-2552, 1997.
76. V.V. Semak, B. Damkroger, S. Kempka, "Temporal evolution of the temperature field in the beam interaction zone during laser material processing," *Journal of Physics D-Applied Physics*, vol. 32, no. 15, pp. 1819-1825, 1999.
77. N.M.B. Bulgakova, A. V., "Pulsed laser ablation of solids: transition from normal vaporization to phase explosion," *Applied Physics a-Materials Science & Processing*, vol. 73, no. 2, pp. 199-208, 2001.
78. W.W. Mullins, "Flattening of a Nearly Plane Solid Surface Due to Capillarity," *Journal of Applied Physics*, vol. 30, no. 1, pp. 77-83, 1959.
79. V. Zandian, J.S. Florry, D. Taylor, "Viscosity of Fused-Silica with Different Hydroxyl Contents," *British Ceramic Transactions and Journal*, vol. 90, no. 2, pp. 59-60, 1991.
80. L. Robin, P. Combis, P. Cormont, L. Gallais, D. Hebert, "Infrared thermometry and interferential microscopy for analysis of crater formation at the surface of fused silica under CO₂ laser irradiation," *Journal of Applied Physics*, vol. 111, no., pp. 063106, 2012.
81. Y.D. Kim, W.S. Kim, "A numerical analysis of heat and fluid flow with a deformable curved free surface in a laser melting process," *International Journal of Heat and Fluid Flow*, vol. 29, no. 5, pp. 1481-1493, 2008.
82. T.D. Bennett, D.J. Krajnovich, C.P. Grigoropoulos, P. Baumgart, A.C. Tam, "Marangoni mechanism in pulsed laser texturing of magnetic disk substrates," *Journal of Heat Transfer-Transactions of the Asme*, vol. 119, no. 3, pp. 589-596, 1997.
83. K. Osawa, H. Inoue, A. Masuno, K. Katayama, Y.J. Zhang, F. Utsuno, Y. Sugahara, K. Koya, A. Fujinoki, H. Tawarayama, H. Kawazoe, "Smoothing of surface of silica glass by heat treatment in wet atmosphere," *Journal of Applied Physics*, vol. 109, no. 10, pp., 2011.
84. T.D. Bennett, D.J. Krajnovich, L. Li, "Thermophysical modeling of bump formation during CO₂ laser texturing of silicate glasses," *Journal of Applied Physics*, vol. 85, no. 1, pp. 153-159, 1999.
85. S.C. Chen, D.G. Cahill, C.P. Grigoropoulos, "Melting and surface deformation in pulsed laser surface micromodification of Ni-P disks," *Journal of Heat Transfer-Transactions of the Asme*, vol. 122, no. 1, pp. 107-112, 2000.
86. E. Mendez, K.M. Nowak, H.J. Baker, F.J. Villarreal, D.R. Hall, "Localized CO₂ laser damage repair of fused silica optics," *Applied Optics*, vol. 45, no. 21, pp. 5358-5367, 2006.
87. K.M. Nowak, H.J. Baker, D.R. Hall, "Efficient laser polishing of silica micro-optic components," *Applied Optics*, vol. 45, no. 1, pp. 162-171, 2006.
88. P. Hrma, W.T. Han, A.R. Cooper, "Thermal Healing of Cracks in Glass," *Journal of Non-Crystalline Solids*, vol. 102, no. 1-3, pp. 88-94, 1988.
89. F.Y. Genin, A. Salleo, T.V. Pistor, L.L. Chase, "Role of light intensification by cracks in optical breakdown on surfaces," *Journal of the Optical Society of America a-Optics Image Science and Vision*, vol. 18, no. 10, pp. 2607-2616, 2001.
90. R.H. Doremus, "Viscosity of silica," *Journal of Applied Physics*, vol. 92, no. 12, pp. 7619-7629, 2002.
91. B.N. Chichkov, C. Momma, S. Nolte, F. vonAlvensleben, A. Tunnermann, "Femtosecond, picosecond and nanosecond laser ablation of solids," *Applied Physics a-Materials Science & Processing*, vol. 63, no. 2, pp. 109-115, 1996.
92. E.G. Gamaly, "The physics of ultra-short laser interaction with solids at non-relativistic intensities," *Physics Reports-Review Section of Physics Letters*, vol. 508, no. 4-5, pp. 91-243, 2011.

93. H.Y. Sohn, "The influence of chemical equilibrium on fluid-solid reaction rates and the falsification of activation energy," *Metallurgical and Materials Transactions B-Process Metallurgy and Materials Processing Science*, vol. 35, no. 1, pp. 121-131, 2004.
94. V. Alexiades, D. Autrique, in: (Ed.)[^](Eds.) Eighth Mississippi State Conference on Differential Equations and Computational Simulations; Electron. J. Diff. Eqns, Starkville, Mississippi, USA, 2009, p 1-14.
95. S. Elhadj, S.R. Qiu, A.M. Monterrosa, C.J. Stolz, "Heating dynamics of CO₂-laser irradiated silica particles with evaporative shrinking: Measurements and modeling," *Journal of Applied Physics*, vol. 111, no. 9, pp., 2012.
96. S.R. Franklin, R.K. Thareja, "Dependence of ablation parameters on the temperature and phase of ablated material," *Journal of Applied Physics*, vol. 93, no. 9, pp. 5763-5768, 2003.
97. V.K. Sysoev, V.I. Masychev, B.P. Papchenko, S.Y. Rusanov, A.A. Yakovlev, N.P. Glukhoedov, "High-rate IR laser evaporation of silica glass," *Inorganic Materials*, vol. 39, no. 5, pp. 532-537, 2003.
98. C. Duty, D. Jean, W.J. Lackey, "Laser chemical vapour deposition: materials, modelling, and process control," *International Materials Reviews*, vol. 46, no. 6, pp. 271-287, 2001.
99. I.P. Herman, "Laser-Assisted Deposition of Thin-Films from Gas-Phase and Surface-Adsorbed Molecules," *Chemical Reviews*, vol. 89, no. 6, pp. 1323-1357, 1989.
100. H.M. Christen, G. Eres, "Recent advances in pulsed-laser deposition of complex oxides," *Journal of Physics-Condensed Matter*, vol. 20, no. 26, pp., 2008.
101. I.A. Shareef, G.W. Rubloff, W.N. Bill, "Role of gas phase reactions in subatmospheric chemical-vapor deposition ozone/TEOS processes for oxide deposition," *Journal of Vacuum Science & Technology B*, vol. 14, no. 2, pp. 772-774, 1996.
102. C.G. Dupuy, J.E. Hurst, "High Spatial-Resolution Infrared-Emission Thermal Measurement of Laser-Induced Chemical Vapor-Deposition," *Review of Scientific Instruments*, vol. 63, no. 7, pp. 3763-3766, 1992.
103. K. Kwok, W.K.S. Chiu, "Investigation of open-air laser-induced chemical vapor deposition of carbon on moving optical fibers," *Optical Engineering*, vol. 44, no. 7, pp. -, 2005.
104. J.S. Han, K.F. Jensen, "Combined Experimental and Modeling Studies of Laser-Assisted Chemical-Vapor-Deposition of Copper from Copper(I)-Hexafluoroacetylacetonate Trimethylvinylsilane," *Journal of Applied Physics*, vol. 75, no. 4, pp. 2240-2250, 1994.
105. D. Bauerle, B. Luk'yanchuk, K. Piglmayer, "On the reaction kinetics in laser-induced pyrolytic chemical processing," *Applied Physics A: Materials Science & Processing*, vol. 50, no. 4, pp. 385-396, 1990.